

# Antiskyrmions and their electrical footprint in crystalline mesoscale structures of $\text{Mn}_{1.4}\text{PtSn}$

Moritz Winter<sup>1,2,3</sup>, Francisco J. T. Goncalves<sup>4</sup>, Ivan Soldatov<sup>5</sup>, Yangkun He<sup>2</sup>,  
Belén E. Zúñiga Céspedes<sup>2,6</sup>, Peter Milde<sup>6</sup>, Kilian Lenz<sup>4</sup>, Sandra Hamann<sup>1</sup>,  
Marc Uhlarz<sup>1</sup>, Praveen Vir<sup>2</sup>, Markus König<sup>2</sup>, Philip J. W. Moll<sup>2,7</sup>, Richard  
Schlitz<sup>8</sup>, Sebastian T. B. Goennenwein<sup>8</sup>, Lukas M. Eng<sup>6,9</sup>, Rudolf Schäfer<sup>5,8</sup>,  
Joachim Wosnitzer<sup>1,8,9</sup>, Claudia Felser<sup>2,9</sup>, Jacob Gayles<sup>2,10,\*</sup>, and Toni Helm<sup>1,2,\*\*</sup>

<sup>1</sup>Dresden High Magnetic Field Laboratory (HLD-EMFL),

Helmholtz-Zentrum Dresden-Rossendorf, 01328 Dresden, Germany.

<sup>2</sup>Max Planck Institute for Chemical Physics of Solids, 01187 Dresden, Germany.

<sup>3</sup>Dresden Center for Nanoanalysis, cfaed, Technical

University Dresden, 01096 Dresden, Germany.

<sup>4</sup>Institute of Ion Beam Physics and Materials Research,

Helmholtz-Zentrum Dresden-Rossendorf, 01328 Dresden, Germany.

<sup>5</sup>Leibniz Institute for Solid State and Materials

Research Dresden, 01069 Dresden, Germany.

<sup>6</sup>Institute of Applied Physics, Technical

University Dresden, 01062 Dresden, Germany.

<sup>7</sup>École Polytechnique Fédérale de Lausanne, 1015 Lausanne, Switzerland.

<sup>8</sup>Institute for Solid State and Materials Physics,

Technical University Dresden, 01062 Dresden, Germany.

<sup>9</sup>Würzburg-Dresden Cluster of Excellence ct.qmat, 01062 Dresden, Germany.

<sup>10</sup>Department of Physics, University of South Florida, Tampa, Florida 33620, USA.

\*E-mail: gayles@usf.edu

\*\*E-mail: t.helm@hzdr.de

## Abstract

Skyrmionic materials hold the potential for future information technologies, such as race-track memories. Key to that advancement are systems that exhibit high tunability and scalability, with stored information being easy to read and write by means of all-electrical techniques. Topological magnetic excitations such as skyrmions and antiskyrmions, give rise to a characteristic topological Hall effect. However, the electrical detection of antiskyrmions, in both thin films and bulk samples has been challenging to date. Here, we apply magneto-optical microscopy combined with electrical transport to explore the antiskyrmion phase as it emerges in crystalline mesoscale structures of the Heusler magnet  $\text{Mn}_{1.4}\text{PtSn}$ . We reveal the Hall signature of antiskyrmions in line with our theoretical model, comprising anomalous and topological components. We examine its dependence on the vertical device thickness, field orientation, and temperature. Our atomistic simulations and experimental anisotropy studies demonstrate the link between antiskyrmions and a complex magnetism that consists of competing ferromagnetic, antiferromagnetic, and chiral exchange interactions, not captured by micromagnetic simulations.

## INTRODUCTION

The field of skyrmionics comprises new phases of magnetic systems, where the individual spins align as whirls [1–4], that hold the potential to advance the understanding of topology in condensed-matter physics. Fundamentally, magnetic textures, such as skyrmions [3, 5], antiskyrmions [6, 7] (ASKs) and related skyrmionic systems [8–10], are distinguished by the relative rotation of the individual magnetic moments with respect to one another in the presence of a magnetically ordered background. This topologically protected state can be used to robustly carry and store high-density information at fast speed with low power consumption, as proposed in

racetrack memory spintronic devices [11, 12]. Solitary skyrmion states as well as crystal lattices of skyrmion systems have been reported for many magnetic crystals that break inversion symmetry such as bulk chiral magnetic compounds [5, 13], multilayer heterostructures [14, 15], thin films [16], oxides [17], and, more recently, tetragonal Heusler systems [6, 18]. While experimental observations from, e.g., Lorentz transmission electron microscopy [6, 19, 20], neutron scattering [5], and magnetic force microscopy [21, 22] have shown great advancement over the last decades, detection by electrical means is required for the realization of energy-efficient spintronic devices [11, 12], probabilistic [23] and neuromorphic computing [24]. Furthermore, a pivotal point for applications is the ability to control and scale skyrmionics [25, 26], or even to transform one species of magnetic texture into another in multiskyrmion systems [18, 27, 28].

The tetragonal Heusler compound  $\text{Mn}_{1.4}\text{PtSn}$  [29] has recently gained a lot of interest as it hosts distinct topological states. Most excitingly, an ASK lattice can be established at room temperature. Besides the high tunability of the Heusler compounds [22, 27, 30], the competition of magnetic exchange interactions and anisotropy lead to an enhanced temperature range over which ASKs can be stabilized in comparison to skyrmion bulk systems. Bulk  $\text{Mn}_{1.4}\text{PtSn}$  displays a complex correlation of exchange between two Mn sublattices that leads to a spin reorientation from a collinear to a noncollinear arrangement at temperatures  $T_{\text{SR}} \approx 170\text{ K}$  and below, which contributes to the anisotropy at low temperatures. At temperatures above the spin reorientation, sophisticated magnetic textures can be realized thanks to the combination of in-plane (perpendicular to the  $c$  axis) and anisotropic Dzyaloshinskii-Moriya interaction (DMI), crystal anisotropy along the tetragonal axis, and dipole-dipole interaction due to large moments ( $> 4\mu_{\text{B}}$ ). Above  $T_{\text{SR}}$ , in the absence of an external magnetic field, the compound prefers a spin-spiral state that is directly connected to the ratio of the exchange interaction and DMI. For a finite range of

external magnetic fields, a long-range ( $> 100$  nm) hexagonal ASK phase as well as a short-range noncoplanar state ( $< 1$  nm) were found [6].

These ASKs exhibit an extraordinary stability to sample-thickness variations to at least a few hundred nanometers confirmed by Lorentz transmission electron microscopy [20] and x-ray studies [31]. The latter confirmed bulk skyrmions in few microns thick samples. The diameter of the ASKs scales linearly with thickness and was found to grow to multiple hundreds of nanometers in micron-sized samples [22, 27]. For very thin platelets, the phase diagram becomes more complex. Multiple skyrmion-like textures that are different above and below  $T_{\text{SR}}$  can be stabilized by varying the field orientation [18, 30]. Surprisingly, neutron-scattering experiments on bulk  $\text{Mn}_{1.4}\text{PtSn}$  did not resolve any ASKs [32]. Even more intriguing, a huge additional component in the Hall effect, associated with a topological origin, emerges in the low-temperature region of the phase diagram, just below  $T_{\text{SR}}$ , exceeding expectations for skyrmions [33]. This is likely related to noncollinear magnetism. Therefore, it is still an open question if and how ASKs contribute to the Hall effect and, in particular, how strong that effect is.

The topological nature of skyrmions and ASKs should be observable in terms of a unique response to an external electric field, i.e., a topological Hall effect (THE) in electrical transport. The THE belongs to the family of Berry-curvature Hall effects [34, 35], where emergent fields due to a real-space variation of the local magnetism, describable by the Berry curvature [36], are the origin of a transverse voltage. Closely related to the THE is the anomalous Hall effect (AHE), due to the interaction of localized and conduction electrons [37]. In a finite magnetic field, the Hall response is a voltage transverse to the applied current. This is sketched in Fig. 1a. Phenomenologically, the total Hall effect can be described by a superposition of three

contributions [37]:

$$\rho_{xy} = \rho_{xy}^{\text{OHE}} + \rho_{xy}^{\text{AHE}} + \rho_{xy}^{\text{THE}}. \quad (1)$$

The ordinary Hall effect (OHE) that scales with the external magnetic field,  $\mathbf{H}$ ; The AHE, which scales with the magnetization  $\mathbf{M}$ , describable in terms of an intrinsic momentum-space Berry curvature and extrinsic scattering mechanisms, such as skew and side-jump scattering [37, 38]; The THE, which can be described in terms of the chiral product:

$$\chi_{ij} = \mathbf{S}_i \cdot (\mathbf{S}_j \times \mathbf{S}_k), \quad (2)$$

where  $\mathbf{S}_i$  is the local spin orientation. The latter may be utilized to identify the sign of the topological charge, being opposite for skyrmions and ASKs, respectively.

In this work, we successfully combined *in-situ* transport with magneto-optical microscopy applied to mesoscale structures fabricated from single-crystals by focused-ion-beam assisted patterning. This approach enables us to directly examine the Hall signature of the ASK phase in Hall-bar devices with thicknesses ranging from 500 nm to 10  $\mu\text{m}$ , observable from  $T_{\text{SR}}$  to room temperature and above. The antiskyrmionic Hall component  $\rho_{xy}^{\text{ASK}} = \rho_{xy}^{\text{AHE}} + \rho_{xy}^{\text{THE}}$  is comprised of an anomalous and a topological component. We study its temperature, field-orientation, and device-thickness dependence. As the expected THE is rather small, we conclude that the major contribution originates from the AHE of the ASKs. In contrast to the general approach of micromagnetic simulations, we apply atomistic spin-dynamic calculations that capture the underlying complex magnetism of  $\text{Mn}_{1.4}\text{PtSn}$ , inevitably linked to the emergence of ASKs at high temperatures. We show experimentally how the periodicity of magnetic textures and the  $\rho_{xy}^{\text{ASK}}$  of ASKs scales with thickness. Our ferromagnetic resonance (FMR) studies reveal the distinct magnetic anisotropies above and below  $T_{\text{SR}}$  that lay the foundation for the emergence of multiple skyrmionic textures reported previously.

## RESULTS AND DISCUSSION

### Room-temperature Hall signature of the antiskyrmion phase

In Fig. 1a, we show a schematic of a step-like device, where an ASK lattice is formed in an external magnetic field applied perpendicular to the  $ab$  plane of the step device (for further details see Supplementary Notes 1-3). ASKs possess an anisotropic winding with a topological charge of opposite sign as compared to isotropic Bloch and Néel skyrmion systems [7]. As the thickness,  $d$ , of a device made from  $\text{Mn}_{1.4}\text{PtSn}$  is reduced the periodicity of the ASK lattice decreases and, hence, the ASK size, too. This in turn increases the density and should, therefore, directly affect the magnitude of the topological charge that contributes to the Hall voltage,  $V_{xy}$ , transverse to the electric current, i.e., the THE. Furthermore, the local net magnetization of an individual ASK is roughly zero. Consequently, the volume magnetization should exhibit a reduction as ASKs emerge. This would affect the anomalous Hall effect, which is proportional to the magnetization [39, 40]. However, direct measurements of the magnetization for sub-micron-thin, small-in-volume samples of  $\text{Mn}_{1.4}\text{PtSn}$  remains a technical challenge.

Figure 1b displays false-color scanning electron microscope images of two different devices fabricated by focussed-ion-beam (FIB) assisted patterning, namely, a step-like device with thicknesses  $d = 11.2, 8.4$ , and  $2.7 \mu\text{m}$  and a standalone device with  $d = 1.0 \mu\text{m}$ . In Fig. 1c, we display the total measured Hall effect for all thicknesses from the demagnetized state ( $\mu_0 H = 0$ ) up to a nearly saturated state ( $H_S$ ). For  $d < 8.4 \mu\text{m}$ , a noticeable hysteresis appears in the Hall effect before saturation, which details a noncoplanar magnetic and ASK spin texture, when the field is applied parallel to the  $c$  axis. Device F with  $d = 0.8 \mu\text{m}$  was set up as a Hall bar to simultaneously measure the Hall voltage while observing the magnetic state *in-situ* via

polar magneto-optical Kerr effect (MOKE) microscopy [41]. Selected MOKE images of the device are presented in Fig. 1d. The Hall data in Fig. 1e was simultaneously measured with polar MOKE microscopy, shown in Fig. 1d as a function of external field. Fig. 1e displays the Hall-resistivity hysteresis loops recorded for the left (red) and the right (black) contacts (shown in Fig. 2f) of device F with the sweep direction indicated by black arrows. The down sweep stays in the saturated state down to approximately 460 mT due to the anisotropy in the magnetic exchange interactions and the critical aspect ratio of the sample that adds an additional shape-anisotropy contribution [22]. However, on the up sweep there are two clearly distinguishable slopes: The first originates from distinct conical magnetic spin spirals formed by the two non-equivalent magnetic Mn sublattices [33]. This hysteresis is also discernible in the magnetization, as we show in Supplementary Note 4. The second, highlighted by the yellow-shaded area, shows a slope change and coincides with the formation of the ASK lattice. The MOKE images of Fig. 1d, recorded simultaneously with the Hall resistivity, show a saturated magnetized state down to above 450 mT, where band domains associated with magnetic spin-spirals suddenly emerge. When increasing field from zero, the conical spin-spiral state starts to slowly disintegrate into individual ASKs and ASK strings. Then suddenly at 535 mT, an ASK lattice emerges, exactly where the shoulder in the Hall resistivity develops. A more refined video sequence that shows a full field scan between saturation and zero field can be found in Supplementary Movie 1. In Supplementary Note 5, we present an additional sequence of MOKE images recorded for device C with  $d = 2.4 \mu\text{m}$  before it was structured into the Hall-bar geometry, where we observed much larger band domains and consequently a less dense ASK lattice.

## The magnetic structure of $\text{Mn}_{1.4}\text{PtSn}$ and the expected transport signature in the ASK phase

In Fig. 2a, we sketch the spin configuration and the respective interactions present in  $\text{Mn}_{1.4}\text{PtSn}$ . The combination of DMI, induced by the  $D_{2d}$  symmetry, FM and AFM interaction, is an ideal foundation for diverse magnetic textures [33]. We find that the physics of topological textures in  $\text{Mn}_{1.4}\text{PtSn}$  can be accurately modeled purely from the exchange interactions and magnetocrystalline anisotropy in three atomic layers of the two magnetic sublattices [10, 42, 43]. More significantly, the ratios of the exchange constants determine the underlying physics; therefore, we tuned the classical parameters in atomistic spin-dynamic simulations to clearly show the effects seen in the experiments. There are three sets of exchange interactions and DMI crucial for the stabilization of in-plane ASKs in  $\text{Mn}_{1.4}\text{PtSn}$ . The first interaction,  $J_1$  between the Mn(1) and Mn(2) sublattice, is ferromagnetic. It reaches along the shortest magnetic distance, where the DMI is strongest. The second ferromagnetic interaction,  $J_2$  between magnetic sublattices of the same type and perpendicular to the  $c$  axis, is the main interaction responsible for the Curie temperature. The interaction  $J_3$  for the Mn sublattice Mn(2) at the Wyckoff position  $4d$  is of AFM nature, and assists in the formation of the noncoplanar structure below  $T_{\text{SR}}$ . These AFM and FM interactions compete to form double-chiral spin spirals in order to minimize the energy. The chirality degeneracy is lifted by the DMI.

The calculated out-of-plane (in-plane) component of the spin-spiral and ASK state is shown in the upper (lower) panel in Fig. 2b and 2c, respectively. The yielded magnetization hysteresis (Fig. 2d) is in line with our experimental observations of a finite hysteresis away from zero field for a transition from the spin-spiral ground state into a stable ASK phase (for further details see Supplementary Note 6). The calculated magnetization exhibits a weak region, that is a shallow slope change right before the



saturation field, consistent with our THE observations (see Fig. 2d). The chiral product,  $\chi_{ij}$  leads to a topological winding number,  $w = 1/4\pi \int \hat{\mathbf{M}} \cdot (\delta_x \hat{\mathbf{M}} \times \delta_y \hat{\mathbf{M}}) dx dy$ , where  $\delta_i = \partial/\partial x_i$ , and  $\hat{\mathbf{M}}(r, t) = \mathbf{M}(r, t)/|\mathbf{M}|$  is the direction of the magnetization at each spatial position. The presence of  $w$  causes an emergent magnetic field,  $H^e = \frac{\hbar}{2} \epsilon_{zxy} \hat{\mathbf{M}} \cdot (\delta_x \hat{\mathbf{M}} \times \delta_y \hat{\mathbf{M}})$ , originating from a real-space Berry curvature [34]. The so-called topological charge,  $q_T$ , is negative for skyrmions and positive for ASKs. Thereby, the THE is a direct link to the topology of the magnetic texture:

$$\rho_{xy}^{\text{THE}} = R_{xy}^{\text{THE}} H^e, \quad (3)$$

where the Hall coefficient,  $R_{xy}^{\text{THE}}$ , is tied to the complex multiorbital electronic structure [44]. The composite nature of  $R_{xy}^{\text{THE}}$  and  $H^e$  complicates the differentiation of skyrmionic configurations with distinct winding numbers across multiple materials. However, in  $\text{Mn}_{1.4}\text{PtSn}$  distinct magnetic textures are induced by the external field.

In the lower panel of Fig. 2d, we plot  $q_T$  against the external field. In the field-up sweep,  $q_T$  in the ASK phase exhibits an opposite sign as compared to the net charge in the low-field spin-spiral phase and extends to higher fields as compared to the reoccurring  $q_T$  in the down sweep (orange curve). The down sweep (black curve) remains flat and only exhibits a positive contribution at lower fields, originating from the reestablishing spin-spiral phase. Hence, the subtraction of field-up and -down sweep mostly cancels out the component from the ordered phase and should, therefore, yield the Hall effect due to ASKs directly. In  $\text{Mn}_{1.4}\text{PtSn}$ , ASK sizes can reach a few hundred nanometers in diameter. For these huge objects the expected THE is rather small [39]. Figures 2e, f, and g provide a comparison of the signatures observed in the Hall resistivity as well as in the magnetization for a  $2.4 \mu\text{m}$  thick lamella sample. The hysteresis shows up for both quantities and a linear fit of the slope in the differences  $\Delta\rho_{xy}$  and  $\Delta M$  just below the saturation field reveals a shoulder-like feature being discernible in both quantities. The insets of Fig. 2g present the contribution

we associate with the presence of ASKs. Apparently, the shoulder can be addressed to an anomalous Hall component due to the emergence of the ASK textures. The magnetic moment scales with the volume of the material and the observed feature in the magnetization is hardly distinguishable from the noise background. We also know that ASKs only show up for micron-thick devices. Therefore, it is hard to trace the ASK feature for smaller thicknesses in the magnetization. Here, the Hall effect appears to be the ideal tool. In Supplementary Note 7 we provide subtraction results from our experimental transport data at various temperatures for device B with  $d = 1\ \mu\text{m}$ . A clear feature can easily be traced upon varying the device thickness, temperature, and field orientation (see the following sections).

### **Thickness- and temperature-dependent Hall effect in the ASK phase**

While MOKE microscopy in combination with electrical transport allows for simultaneous measurements of the magnetic texture and the Hall effect in  $\text{Mn}_{1.4}\text{PtSn}$ , it is limited in spatial resolution by the wavelength of the optical light used [41]. We, therefore, use magnetic force microscopy (MFM) to resolve the ASK lattice induced in samples of different thickness  $d$ . Figure 3a shows MFM images at zero and 0.55 T for a  $5\ \mu\text{m}$  and  $1.5\ \mu\text{m}$  thick sample. The spin-spiral domain bands and the ASK lattice are discernible with varying periodicity, depending on  $d$  (the lower  $d$  the smaller the magnetic periodicity). The fast Fourier transforms (FFTs), shown in the lower panels in Fig. 3a, highlight the change in topology as the system transforms from the spin-spiral into the hexagonal ASK phase. The size and periodicity of the ASKs are affected by the thickness as has been shown recently—the latter varies almost linearly with thickness [22, 32].

This suggests that a THE induced by ASKs is expected to grow quadratically with decreasing  $d$ , as it is directly related to the ASK density, which is in turn

proportional to the area occupied by each ASK. In Fig. 3b, we show  $\rho_{xy}^{\text{ASK}}$  at room temperature determined for various devices with different thicknesses between 2.4 and 0.8  $\mu\text{m}$ . The overall magnitude varies between 40 and 50 n $\Omega\text{cm}$ . We also studied the thickness dependence in more depth on transport devices E and G, presented in Fig. 3c. In these cases, we lowered the thickness by low-energy (5 kV) Ar-ion etching in steps and measured the room-temperature Hall effect after each thinning step. The overall trend of an increased response for smaller thickness is apparent. However, this may also originate from an increasing number of ASKs that can emerge in between the electrical Hall contacts due to their shrinking diameters upon device-thickness reduction. As was shown already for Néel skyrmions in Co nanolayers, the AHE of single skyrmions may be much stronger than the THE component [39]. Therefore, at this point, we can only provide an upper estimate of the THE: Namely, it must be smaller than a fraction of the magnitude of the detected  $\rho_{xy}^{\text{ASK}}$ . In Supplementary Note 7 we provide a theoretical estimate following the previous approaches [5, 44] for a known ASK density. For our microscale devices the ASK size is approximately 100 nm, which would lead to a theoretically expected THE component of  $|\rho^{\text{THE}}| \sim 50 \text{ n}\Omega\text{cm}$ .

Moreover, we find that  $\rho_{xy}^{\text{ASK}}$  remains as pronounced as at room temperature all the way down to temperatures close to  $T_{\text{SR}}$  (see Fig. 3d and Supplementary Note 7). Below  $T_{\text{SR}}$ , it is strongly suppressed until it vanishes and additional step-like jumps in the Hall resistivity occur. The saturation field marks the upper boundary of the ASK field region (yellow). With decreasing temperature, it shifts towards higher values until saturating near  $T_{\text{SR}}$ , where noncoplanar magnetism starts to take over. Its overall amplitude starts to subside around  $T_{\text{SR}}$  as can be seen from Fig. 3e. Below 150 K, we cannot unambiguously link the observed deviations to skyrmions. To visualize the crossover around  $T_{\text{SR}}$  we show the maximum  $\Delta\rho_{xy}$  plotted against the temperature in Fig. 3f. This demonstrates the gradual change of the overall behavior of

the observed hysteresis near the spin-reorientation transition region (shaded region) associated with the onset of noncoplanar order and a reorientation of the magnetic easy axis. Further microscopic and spectroscopic studies are highly desirable in order to understand the details of the temperature dependence.

### **Emergence of a new state below $T_{\text{SR}}$**

Below  $T_{\text{SR}}$ , the overall Hall response decreases more rapidly and the hysteresis in field narrows (see Fig. 4a). We present a detailed angular study on device B in Supplementary Note 8. As we tilt the magnetic field away from  $H \parallel c$ , the hysteresis subsides (it is absent in the high-temperature curves shown in Fig. 4b). For temperatures near and below  $T_{\text{SR}}$  and the field being oriented away from the  $c$  direction, we observe a prominent hump-like enhancement of  $\rho_{xy}(H)$  close to the saturation field (see for example the maximum in  $\rho_{xy}(H)$  at 180 K and  $H \parallel b$  in Fig. 4b). This feature was already explored for bulk samples [29, 33]. Its origin is a THE linked to the establishment of a noncoplanar spin structure with a strong real-space Berry curvature. Excitingly, for fields along the  $b$  axis,  $\rho_{xy}(H)$  starts acquiring a negative high-field slope and even changes sign at low temperatures (Fig. 4b). At 2 K, we observe a surprisingly large transverse transport signal even without any out-of-plane field component. For angles within only a few degrees off the in-plane orientation (i.e.,  $\theta = 90^\circ$ ) it is accompanied by a new hysteresis that exhibits opposite sign as compared to the one for  $H \parallel c$ . As we fine-tune the angular step width, we observe a hysteresis that extends to fields even larger than 4 T, being extremely sensitive to minute changes in  $\theta$  (see Supplementary Note 8). Moreover, step-like changes in the hysteretic part of  $\rho_{xy}(H)$  occur (see for example the 150 K curve in Fig. 4b). Hence, our data indicates an intriguing magnetic behavior for low temperature and field aligned within the  $ab$  planes, likely originating from the

noncoplanar magnetism with a much stronger magnetocrystalline anisotropy for low temperatures. As we show in Fig. 4d and Supplementary Note 8, both the AHE and the OHE deviate from the conventional  $\cos\theta$  dependence, observable at room temperature, as temperature is tuned to  $T_{\text{SR}}$  and below (see red dashed fits). This further indicates an enhanced saturation field for the in-plane field orientation. These temperature- and angle-dependent changes are independent of the device thickness (confirmed for devices A, B, and C).

To further explore the temperature-dependent change in the magnetic exchange interactions we conducted fixed-frequency FMR experiments on a thin ( $\sim 800$  nm) lamella sample. In Fig. 4e, we present FMR spectra recorded at 260 and 10 K for two field directions each. The spectra were recorded while sweeping the field from the negative field-polarized state to the positive side and back, i.e., following the Hall-effect hysteresis curves. For further details, see also Supplementary Note 9. We also observe the hysteresis around 0.5 T for  $H \parallel c$  in the FMR data (see black curve in Fig. 4e and inset). Furthermore, at 260 K, we observe one narrow resonance mode attributed to the field-polarized state. As we tilt the field towards  $H \parallel b$ , the resonance preserves its narrow shape and the nearly isotropic angular dependence, varying between 0.62 and 0.75 T. This suggests that above  $T_{\text{SR}}$ , the magnetocrystalline anisotropy is weak. The maximum resonance field (corresponding to a magnetically hard axis) occurs around  $24^\circ$ . An approximate fit to the angle-dependent data yields a weak effective in-plane-anisotropy field, which is comparable in magnitude to the ASK compound  $\text{Fe}_{1.9}\text{Ni}_{0.9}\text{Pd}_{0.2}\text{P}$  [28]. At temperatures well below  $T_{\text{SR}}$ , the main resonance mode becomes broad for  $H \parallel c$  and asymmetric. In Fig. 4f, the error bars represent the resonance linewidth (half width at half maximum). Such a linewidth broadening is typical for the so-called field dragging, i.e., when  $H$  is not parallel to  $M$  due to a nonuniform magnetization for example. We observe that for high tilt angles close to the  $b$  axis the resonances become narrower and shift to much

lower fields of 0.1 T. The overall angular dependence indicates that the anisotropy is much stronger below  $T_{\text{SR}}$ . These significant changes in the magnetic anisotropies can explain the previously reported vanishing of ASKs and emergence of Bloch-type skyrmions at low temperatures [30]. In addition, the observed hysteresis in transport at high fields indicates new hard-magnetic behavior for the in-plane field orientation. This, therefore, may provide the right environment of the establishment of other distinct skyrmionics, e.g., AFM bimerons [45].

## CONCLUSION

In summary, we demonstrated the direct detection of the Hall resistivity due to the emergence of ASKs in the Heusler compound  $\text{Mn}_{1.4}\text{PtSn}$  by combining electrical transport with magneto-optical microscopy, in line with our theoretical model. Our studies of transport, magnetization, and ferromagnetic resonance reveal a semi-hard magnetic phase, and, hence, the unique link of ASKs to anisotropies, not possible in the cubic B20 compounds with weak anisotropy. We find this semi-hard magnetic behavior to strengthen as we reduce the thickness of the sample, which is particularly interesting for scalable electronic devices [46–48]. Many hard magnetic materials are strongly susceptible to finite sizes and may display nontrivial magnetic textures detectable by Hall transport [24, 49]. As the thickness is decreased, the density of ASKs increases, which we observe directly using MFM, leading to an increase in the Hall-effect signature. Our theoretical prediction of the ASK THE magnitude matches the observed Hall signature values, thereby displaying the importance of the electronic structure for the unexpectedly large Hall signature. However, the disentanglement of the anomalous and topological Hall contributions remains a challenge, without spin-resolved visualization capabilities. In addition, the temperature dependence of the magnetic anisotropy, reflected in our Hall and FMR results, reveals the intimate

link to the crystalline, electronic, and magnetic structure. Our atomistic model, solely based on the competing magnetic exchange interactions, captures the mechanism behind the emergence of ASKs in  $\text{Mn}_{1.4}\text{PtSn}$ . The novelty of tunability of texture sizes and the importance of the exchange interactions offers additional ways to manipulate and detect ASKs. Yet, smaller sizes and new materials with enhanced THE are desirable. Our observations offers a route to room-temperature skyrmionic applications based on multiple distinct types of skyrmionic textures.

## METHODS

**Experimental Design.** The objectives of this study were to visualize the emergence of ASKs in mesoscale devices that allow a simultaneous investigation of the electrical transport under the influence of an external magnetic field and disentangle other contributions to the electrical-transport signature related to the complex magnetism of the multiskyrmion host compound  $\text{Mn}_{1.4}\text{PtSn}$ . We conducted polar magneto-optical Kerr microscopy as well as magnetic force microscopy on micron-sized samples fabricated by focussed-ion-beam assisted patterning. The former microscopy technique was successfully applied for the *in-situ* detection of the Hall effect at room temperature. Furthermore, a detailed study of the ASK Hall signature depending on sample thickness, field orientation, and temperature was conducted. Chip-based FMR measurements depending on temperature, field, and angle were performed to obtain information on the ferromagnetic component of the complex magnetic background around temperatures at which the THE, associated with ASKs, is subsiding.

**Crystal growth.** Single-crystals were prepared by flux-growth technique showing no microtwinning confirmed by Laue diffraction. Details can be found elsewhere [29].

**FIB microfabrication.** We fabricated transport devices from high-quality single crystals of  $\text{Mn}_{1.4}\text{PtSn}$  by the application of Ga or Xe FIB microstructuring, which enable high-resolution investigations of anisotropic transport. FIB micromachining has already proven extremely powerful in various other metallic compounds. A detailed description of the fabrication is provided in Supplementary Note 1 and 2. Further details on FIB-patterned transport devices can be found in previous works of some of the authors [50, 51]. Thin (few microns thick) lamella-shaped slices of  $\text{Mn}_{1.4}\text{PtSn}$  were separated with FIB and manually transferred ex-situ onto a sapphire substrate into a thin layer of insulating two-component epoxy. We then deposited a 100 nm thick gold (Au) layer on top in order to electrically connect the leads with the crystal. With the help of FIB, we thereafter patterned the Au interfaces into separate terminals. In a next step, we removed the Au from the central area of the slice before cutting the lamellae into Hall-bar-shaped transport devices, highlighted by purple color in Fig. 1b. For device A, shown in Fig. 1b, the thin slice of the crystal was polished stepwise to three different thicknesses by FIB before the transfer onto the substrate. This way, a microstructure device was created with three 3-point hall-bar devices connected in series.

**Magnetotransport measurements.** We conducted electrical-transport measurements in a 14 T Quantum Design physical properties measurement system by applying a standard a.c. lock-in technique. A SynkTek multichannel lock-in amplifier as well as Zürich Instruments lock-in amplifiers were used. The current is directed through the FIB cut microstructures (see purple colored parts in Fig. 1b). Dimension of the devices were determined using a scanning electron microscope.

**Magnetic force microscopy.** MFM measurements were performed in two instruments. For room-temperature measurements without external fields we used a Park Systems NX10 with MFM probes from Nanosensors at lift heights between 100 and 150 nm. For measurements under magnetic fields, we used a AIST-NT Smart-



SPM 1000 with MFM probes from Nanosensors at lift heights between 250 and 350 nm together with a Nd-based permanent magnet. The magnetic flux strength was measured at the position of the sample with a MAGSYS HGM09s magnetometer. All data analysis was performed with the Gwyddion software.

**Polar magneto-optical Kerr microscopy.** Experiments were conducted with an AxioScope-type Carl Zeiss wide-field polarization microscope at room temperature. The sample was placed onto the pole of a solenoid-type, water-cooled electromagnet with a maximum magnetic field of 1.5 T aligned along the  $c$  axis. Special care was taken to remove parasitic Faraday contributions by the application of a motorized analyzer. Further details of the method can be found elsewhere [41].

**Ferromagnetic Resonance.** A broadband frequency vector network analyzer (VNA) [52] was used to probe the resonance properties of a  $\text{Mn}_{1.4}\text{PtSn}$  lamella ( $20 \times 100 \times 0.8$ )  $\mu\text{m}^3$  prepared by FIB. A 20  $\mu\text{m}$  wide coplanar wave guide was used for the transmission in an impedance-matched ( $50 \Omega$ ) chip-carrier design. The detection of the FMR modes was carried out via the change in the forward transmission parameter  $S_{21}$  using a Keysight N5225A VNA. Field- and temperature-dependent measurements were performed in an Attocube DRY 1100 cryostat with a split-coil magnet at constant temperature and fixed frequency of 20 GHz using 10 dBm microwave input power. At each field step, the real and imaginary components of the  $S_{21}$  parameter were recorded, using 100 times averaging.

**Numerical calculations.** First-principle calculations were performed on  $\text{Mn}_{1.4}\text{PtSn}$  by using the full-potential linearized augmented plane-wave code FLEUR following the work of Vir et al. [33]. From this, exchange parameters were extracted, where the largest interactions were  $J_1$ ,  $J_2$ ,  $J_3$ , and  $D$ . The atomistic spin calculations were performed in the code VAMPIRE for a lattice with  $372 \times 372$  unit cells [53]. For computation efficiency the Heisenberg exchange parameters are decreased ( $J_1 = 10$  meV,  $J_2 = 12.0$  meV,  $J_3 = -4$  meV) and the DMI magnitude increased ( $D_1 = 2.0$  meV).

The magnetocrystalline anisotropy is single axis and was chosen to be  $0.5\,\mu\text{eV}$ . To simulate the effect of the spin-reorientation transition, we set  $J_3 = -2\,\text{meV}$ . We used the Landau-Lifshitz-Gilbert equation to study the spin dynamics of the system.

## ACKNOWLEDGEMENTS

We would like to acknowledge K. Geishendorf from IFW for his help with transport-device fabrications. Furthermore, we thank A. P. Mackenzie from MPI CPfS and R. Huebner from IBC, HZDR for their support. We are thankful for the help of R. Narkovic and R. Illing from HZDR with the preparation of the substrate used in the FMR experiments. We acknowledge the support of the HLD at HZDR, member of the European Magnetic Field Laboratory (EMFL). We thank the department of A. Mackenzie at MPI CPfS in Dresden and the IBC at HZDR in Dresden for providing access and support to their FIB system. B.E.Z.C. acknowledges support from the International Max Planck Research School for Chemistry and Physics of Quantum Materials (IMPRS-CPQM). P.M. and L.M.E. acknowledges support by the German Research Foundation (DFG) under Grants No. EN 434/38-1 and MI 2004/3-1 as well as EN 434/40-1 as part of the Priority Program SPP 2137 “Skyrmionics”. We acknowledge support by the Collaborative Research Center SFB 1143 (project-id 247310070) and the Würzburg-Dresden Cluster of Excellence on Complexity and Topology in Quantum Matter – *ct.qmat* (EXC 2147, project-id 390858490). P.J.W.M. acknowledges support by the European Research Council (ERC) under the European Union’s Horizon 2020 research and innovation program (grant no. 715730, MiTopMat).

## **AUTHOR CONTRIBUTIONS**

Single-crystal growth and characterization: PV  
FIB microstructure fabrication: TH  
Magnetotransport experiments: MW, SH, MU, RS, TH  
SQUID VSM measurements: YH  
MFM measurements: BEZC, PM  
MOKE microscopy: IS, RS, YH  
FMR measurements: FJTG, KL  
First principle and atomistic spin dynamic simulations: JG  
Supervision: TH, JW, CF, LME, RS, MK, KL, STBG, JG  
Writing and editing of the original draft: All authors

## **COMPETING INTERESTS**

The authors declare no competing interests.

## **DATA AVAILABILITY**

All data supporting the findings of this study are included in the main text and Supplementary Information. Raw data in ASCII format will be provided by the corresponding author upon reasonable request.

## **SUPPLEMENTARY MATERIALS**

In addition, we provide the following supplementary material:

Supplementary Notes (1 to 9)

Supplementary Figures (S1 to S16)

## REFERENCES

---

- [1] Bogdanov, A. N. & Yablonskii, D. A. Thermodynamically stable "vortices" in magnetically ordered crystals. The mixed state of magnets. *Zh. Eksp. Teor. Fiz.* **95**, 178–182 (1989). URL <http://www.jetp.ras.ru/cgi-bin/e/index/e/68/1/p101?a=list>.
- [2] Bogdanov, A. N. & Hubert, A. Thermodynamically stable magnetic vortex states in magnetic crystals. *J. Magn. Magn. Mater.* **138**, 255–269 (1994). URL [https://doi.org/10.1016/0304-8853\(94\)90046-9](https://doi.org/10.1016/0304-8853(94)90046-9).
- [3] Rößler, U. K., Bogdanov, A. N. & Pfleiderer, C. Spontaneous skyrmion ground states in magnetic metals. *Nature* **442**, 797–801 (2006). URL <https://doi.org/10.1038/nature05056>.
- [4] Back, C. *et al.* The 2020 skyrmionics roadmap. *J. Phys. D: Appl. Phys.* **53**, 363001 (2020). URL <https://doi.org/10.1088/1361-6463/ab8418>.
- [5] Mühlbauer, S. *et al.* Skyrmion Lattice in a Chiral Magnet. *Science* **323**, 915–919 (2009). URL <https://www.science.org/doi/abs/10.1126/science.1166767>.
- [6] Nayak, A. K. *et al.* Magnetic antiskyrmions above room temperature in tetragonal Heusler materials. *Nature* **548**, 561 (2017). URL <https://doi.org/10.1038/nature23466>.
- [7] Koshibae, W. & Nagaosa, N. Theory of antiskyrmions in magnets. *Nat. Commun.* **7**, 10542 (2021). URL <https://doi.org/10.1038/ncomms10542>.
- [8] Rybakov, F. N., Borisov, A. B., Blügel, S. & Kiselev, N. S. New Type of Stable Particlelike States in Chiral Magnets. *Phys. Rev. Lett.* **115**, 117201 (2015). URL <https://link.aps.org/doi/10.1103/PhysRevLett.115.117201>.
- [9] Everschor-Sitte, K., Masell, J., Reeve, R. M. & Kläui, M. Perspective: Magnetic

- skyrmions—Overview of recent progress in an active research field. *J. Appl. Phys.* **124**, 240901 (2018). URL <https://doi.org/10.1063/1.5048972>.
- [10] Göbel, B., Mertig, I. & Tretiakov, O. A. Beyond skyrmions: Review and perspectives of alternative magnetic quasiparticles. *Phys. Rep.* **895**, 1–28 (2021). URL <https://www.sciencedirect.com/science/article/pii/S0370157320303525>.
- [11] Nagaosa, N. & Tokura, Y. Topological properties and dynamics of magnetic skyrmions. *Nat. Nanotechnol.* **8**, 899–911 (2013). URL <https://doi.org/10.1038/nnano.2013.243>.
- [12] Parkin, S. S. P. & Yang, S.-H. Memory on the racetrack. *Nat. Nanotechnol.* **10**, 195–198 (2015). URL <http://www.nature.com/doifinder/10.1038/nnano.2015.41>.
- [13] Neubauer, A. *et al.* Topological Hall Effect in the *A* Phase of MnSi. *Phys. Rev. Lett.* **102**, 186602 (2009). URL <https://link.aps.org/doi/10.1103/PhysRevLett.102.186602>.
- [14] Yang, M. *et al.* Creation of skyrmions in van der Waals ferromagnet Fe<sub>3</sub>GeTe<sub>2</sub> on (Co/Pd)<sub>*n*</sub> superlattice. *Sci. Adv.* **6** (2020). URL <https://advances.sciencemag.org/content/6/36/eabb5157>.
- [15] Moreau-Luchaire, C. *et al.* Additive interfacial chiral interaction in multilayers for stabilization of small individual skyrmions at room temperature. *Nat. Nanotechnol.* **11**, 444–448 (2016). URL <https://doi.org/10.1038/nnano.2015.313>.
- [16] Yu, X. Z. *et al.* Near room-temperature formation of a skyrmion crystal in thin-films of the helimagnet FeGe. *Nat. Mater.* **10**, 106–109 (2011). URL <https://doi.org/10.1038/nmat2916>.
- [17] Seki, S., Yu, X. Z., Ishiwata, S. & Tokura, Y. Observation of skyrmions in a multi-ferroic material. *Science* **336**, 198–201 (2012). URL <https://science.sciencemag.org/content/336/6078/198>.
- [18] Jena, J. *et al.* Elliptical Bloch skyrmion chiral twins in an antiskyrmion system. *Nat.*

- Commun.* **11**, 1115 (2020). URL <https://doi.org/10.1038/s41467-020-14925-6>.
- [19] Shimojima, T. *et al.* Nano-to-micro spatiotemporal imaging of magnetic skyrmion's life cycle. *Science Advances* **7** (2021). URL <https://advances.sciencemag.org/content/7/25/eabg1322>.
- [20] Saha, R. *et al.* Intrinsic stability of magnetic anti-skyrmions in the tetragonal inverse Heusler compound  $\text{Mn}_{1.4}\text{Pt}_{0.9}\text{Pd}_{0.1}\text{Sn}$ . *Nat. Commun.* **10**, 1–7 (2019). URL <https://doi.org/10.1038/s41467-019-13323-x>.
- [21] Milde, P. *et al.* Unwinding of a skyrmion lattice by magnetic monopoles. *Science* **340**, 1076–1080 (2013). URL <https://science.sciencemag.org/content/340/6136/1076>.
- [22] Zuniga Cespedes, B. E., Vir, P., Milde, P., Felser, C. & Eng, L. M. Critical sample aspect ratio and magnetic field dependence for antiskyrmion formation in  $\text{Mn}_{1.4}\text{PtSn}$  single crystals. *Phys. Rev. B* **103**, 184411 (2021). URL <https://link.aps.org/doi/10.1103/PhysRevB.103.184411>.
- [23] Zázvorka, J. *et al.* Thermal skyrmion diffusion used in a reshuffler device. *Nat. Nanotechnol.* **14**, 658–661 (2019). URL <https://doi.org/10.1038/s41565-019-0436-8>.
- [24] Song, K. M. *et al.* Skyrmion-based artificial synapses for neuromorphic computing. *Nat. Electron.* **3**, 148–155 (2020). URL <https://doi.org/10.1038/s41928-020-0385-0>.
- [25] Yu, X. Z. *et al.* Motion tracking of 80-nm-size skyrmions upon directional current injections. *Sci. Adv.* **6** (2020). URL <https://advances.sciencemag.org/content/6/25/eaaz9744>.
- [26] Han, M.-G. *et al.* Scaling, rotation, and channeling behavior of helical and skyrmion spin textures in thin films of Te-doped  $\text{Cu}_2\text{OSeO}_3$ . *Sci. Adv.* **6** (2020). URL <https://advances.sciencemag.org/content/6/13/eaax2138>.

- [27] Ma, T. *et al.* Tunable Magnetic Antiskyrmion Size and Helical Period from Nanometers to Micrometers in a D2d Heusler Compound. *Adv. Mater.* **32**, 2002043 (2020). URL <https://onlinelibrary.wiley.com/doi/abs/10.1002/adma.202002043>.
- [28] Karube, K. *et al.* Engineering chiral and topological orbital magnetism of domain walls and skyrmions. *Nat. Mater.* **20**, 335–340 (2021). URL <https://doi.org/10.1038/s41563-020-00898-w>.
- [29] Vir, P. *et al.* Tetragonal Superstructure of the Antiskyrmion Hosting Heusler Compound  $\text{Mn}_{1.4}\text{PtSn}$ . *Chem. Mater.* **31**, 5876–5880 (2019). URL <https://doi.org/10.1021/acs.chemmater.9b02013>.
- [30] Peng, L. *et al.* Controlled transformation of skyrmions and antiskyrmions in a non-centrosymmetric magnet. *Nat. Nanotechnol.* **15**, 181–186 (2020). URL <https://doi.org/10.1038/s41565-019-0616-6>.
- [31] Seki, S. *et al.* Direct visualization of the three-dimensional shape of skyrmion strings in a noncentrosymmetric magnet. *Nature materials* **21**, 181–187 (2022). URL <https://doi.org/10.1038/s41563-021-01141-w>.
- [32] Sukhanov, A. S. *et al.* Anisotropic fractal magnetic domain pattern in bulk  $\text{Mn}_{1.4}\text{PtSn}$ . *Phys. Rev. B* **102**, 174447 (2020). URL <https://link.aps.org/doi/10.1103/PhysRevB.102.174447>.
- [33] Vir, P. *et al.* Anisotropic topological Hall effect with real and momentum space Berry curvature in the antiskymion-hosting Heusler compound  $\text{Mn}_{1.4}\text{PtSn}$ . *Phys. Rev. B* **99**, 140406 (2019). URL <https://link.aps.org/doi/10.1103/PhysRevB.99.140406>.
- [34] Lux, F. R., Freimuth, F., Blügel, S. & Mokrousov, Y. Engineering chiral and topological orbital magnetism of domain walls and skyrmions. *Commun. Phys.* **1**, 60 (2018). URL <https://doi.org/10.1038/s42005-018-0055-y>.
- [35] Lux, F. R., Freimuth, F., Blügel, S. & Mokrousov, Y. Chiral Hall Effect in Noncollinear

- Magnets from a Cyclic Cohomology Approach. *Phys. Rev. Lett.* **124**, 096602 (2020). URL <https://link.aps.org/doi/10.1103/PhysRevLett.124.096602>.
- [36] Berry, M. V. Quantal phase factors accompanying adiabatic changes. *Proc. R. Soc. Lond.* **392**, 45–57 (1984). URL <https://doi.org/10.1098/rspa.1984.0023>.
- [37] Nagaosa, N., Sinova, J., Onoda, S., MacDonald, A. H. & Ong, N. P. Anomalous Hall effect. *Rev. Mod. Phys.* **82**, 1539–1592 (2010). URL <https://link.aps.org/doi/10.1103/RevModPhys.82.1539>.
- [38] Bruno, P., Dugaev, V. K. & Taillefer, M. Topological Hall Effect and Berry Phase in Magnetic Nanostructures. *Phys. Rev. Lett.* **93**, 096806 (2004). URL <https://link.aps.org/doi/10.1103/PhysRevLett.93.096806>.
- [39] Zeissler, K. *et al.* Discrete Hall resistivity contribution from Néel skyrmions in multilayer nanodiscs. *Nat. Nanotechnol.* **13**, 1161–1166 (2018). URL <https://doi.org/10.1038/s41565-018-0268-y>.
- [40] Maccariello, D. *et al.* Electrical detection of single magnetic skyrmions in metallic multilayers at room temperature. *Nat. Nanotechnol.* **13**, 233–237 (2018). URL <https://doi.org/10.1038/s41565-017-0044-4>.
- [41] Soldatov, I. V., Jiang, W., te Velthuis, S. G. E., Hoffmann, A. & Schäfer, R. Size analysis of sub-resolution objects by Kerr microscopy. *Applied Physics Letters* **112**, 262404 (2018). URL <https://doi.org/10.1063/1.5027539>.
- [42] Akosa, C. A., Tretiakov, O. A., Tatara, G. & Manchon, A. Theory of the Topological Spin Hall Effect in Antiferromagnetic Skyrmions: Impact on Current-Induced Motion. *Phys. Rev. Lett.* **121**, 097204 (2018). URL <https://link.aps.org/doi/10.1103/PhysRevLett.121.097204>.
- [43] Caretta, L. *et al.* Fast current-driven domain walls and small skyrmions in a compensated ferrimagnet. *Nat. Nanotechnol.* **13**, 1154–1160 (2018). URL <https://doi.org/10.1038/s41565-018-0255-3>.



- [44] Spencer, C. S. *et al.* Helical magnetic structure and the anomalous and topological hall effects in epitaxial B20  $\text{Fe}_{1-y}\text{Co}_y\text{Ge}$  films. *Phys. Rev. B* **97**, 214406 (2018). URL <https://link.aps.org/doi/10.1103/PhysRevB.97.214406>.
- [45] Göbel, B., Mook, A., Henk, J., Mertig, I. & Tretiakov, O. A. Magnetic bimerons as skyrmion analogues in in-plane magnets. *Phys. Rev. B* **99**, 060407 (2019). URL <https://link.aps.org/doi/10.1103/PhysRevB.99.060407>.
- [46] He, Y. *et al.* A New Highly Anisotropic Rh-Based Heusler Compound for Magnetic Recording. *Adv. Mater.* **32**, 2004331 (2020). URL <https://onlinelibrary.wiley.com/doi/abs/10.1002/adma.202004331>.
- [47] He, Y. *et al.* Topological Hall effect arising from the mesoscopic and microscopic non-coplanar magnetic structure in MnBi. *Acta Materialia* **226**, 117619 (2022). URL <https://www.sciencedirect.com/science/article/pii/S1359645422000039>.
- [48] Wu, H. *et al.* Observation of skyrmion-like magnetism in magnetic Weyl semimetal  $\text{Co}_3\text{Sn}_2\text{S}_2$ . *Mater. Today Phys.* **12**, 100189 (2020). URL <https://www.sciencedirect.com/science/article/pii/S2542529320300134>.
- [49] Sokolov, D. A. *et al.* Metamagnetic texture in a polar antiferromagnet. *Nat. Phys.* **15**, 671–677 (2019). URL <https://doi.org/10.1038/s41567-019-0501-0>.
- [50] Moll, P. J. W. Focused Ion Beam Microstructuring of Quantum Matter. *Annu. Rev. Condens. Matter Phys.* **9**, 147–162 (2018). URL <https://doi.org/10.1146/annurev-conmatphys-033117-054021>.
- [51] Ronning, F. *et al.* Electronic in-plane symmetry breaking at field-tuned quantum criticality in  $\text{CeRhIn}_5$ . *Nature* **548**, 313–317 (2017). URL <http://www.nature.com/doi/10.1038/nature23315><http://www.nature.com/articles/nature23315>.
- [52] Goncalves, F. J. T. *et al.* Collective resonant dynamics of the chiral spin soliton lattice in a monoaxial chiral magnetic crystal. *Phys. Rev. B* **95**, 104415 (2017). URL

<https://link.aps.org/doi/10.1103/PhysRevB.95.104415>.

- [53] Svekis, P. *et al.* Role of Magnetic Exchange Interactions in Chiral-Type Hall Effects of Epitaxial Mn<sub>x</sub>PtSn Films. *ACS Appl. Electron. Mater.* **3**, 1323–1333 (2021). URL <https://doi.org/10.1021/acsaelm.0c01104>.

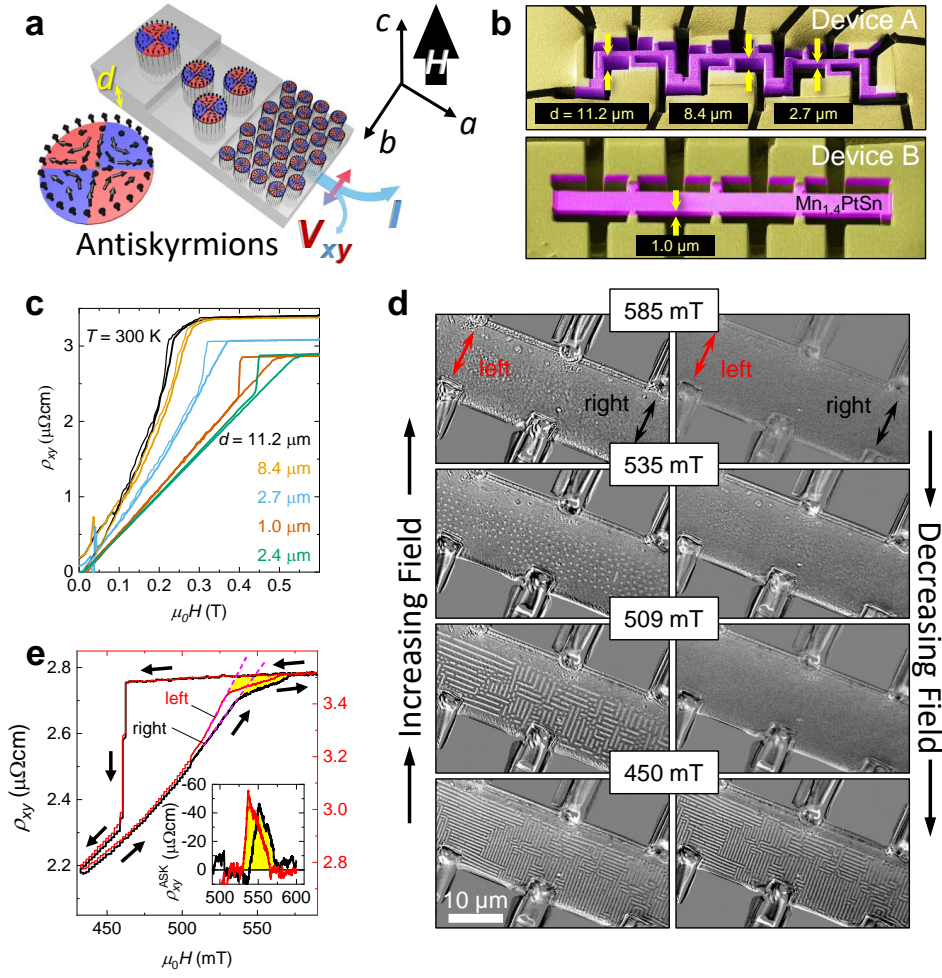


FIG. 1. **Transport signature of ASKs in micro-fabricated  $\text{Mn}_{1.4}\text{PtSn}$  devices.**

(a) Schematic visualization of thickness-dependent ASKs induced by magnetic field,  $H \parallel c$  axis, in a step-like sample with applied current along the  $a$  axis. (b) False-color SEM images of FIB devices A and B with meander-shape (three thicknesses:  $d = 11.2$ ,  $8.4$ , and  $2.7 \mu\text{m}$ ) and Hall-bar geometry ( $d = 1.0 \mu\text{m}$ ), respectively, contacted via sputter-deposited gold contacts. (Further details of all investigated devices, dimensions, and fabrication are presented in Supplementary Notes 1-3). (c) Hall-resistivity loop of samples A, B, and C with different thicknesses,  $d$ , along the  $c$  direction with  $H \parallel c$  at  $T = 300 \text{ K}$ . (d) Greyscale MOKE images of Hall-bar transport device F ( $d = 0.8 \mu\text{m}$ ) at four different fields for up and down sweep, respectively. (e) *In-situ* Hall loop for the left and right contacts of device F marked by red and black color, respectively.

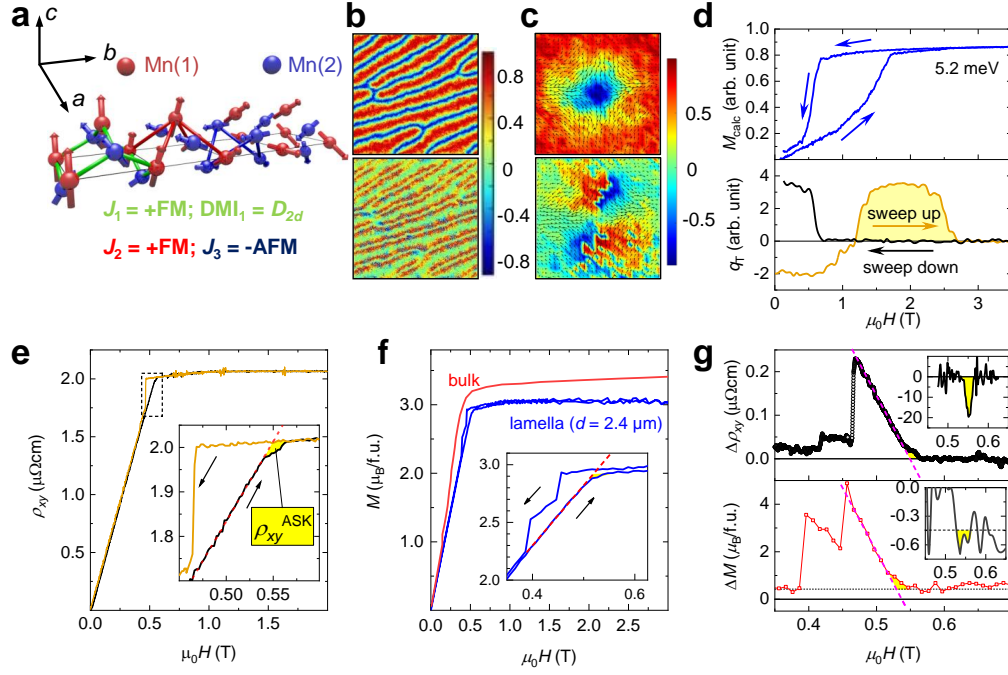
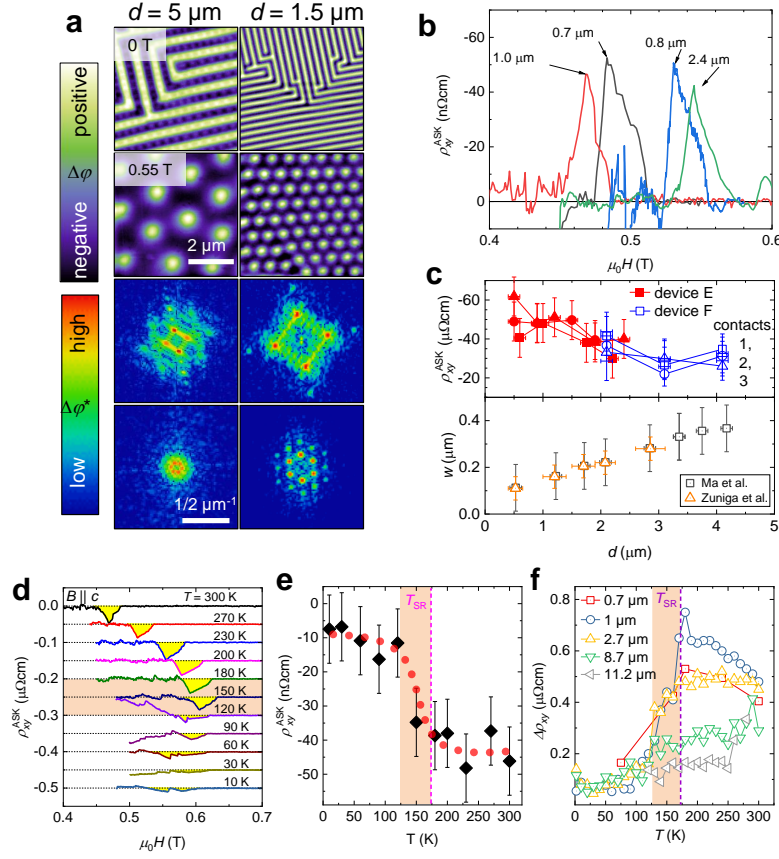


FIG. 2. **Magnetic structure of  $\text{Mn}_{1.4}\text{PtSn}$ .** (a) Sketch of the relevant interaction and coupling constants linking the two Mn sublattices (red and blue). (b), (c) Atomistic spin-dynamic simulations for  $H \parallel c$ : Color maps for an array of  $(372 \times 372)$  unit cells showing the perpendicular  $z$  component in the spin-spiral phase (left) and ASK phase (right), respectively. Black arrows represent the in-plane component. The color scale is given in radiant, where 1/-1 corresponds to a spin alignment parallel/antiparallel to the normal. Lower panels show the in-plane spin-winding component. (d) Upper panel: Calculated magnetization loop for fixed temperature given in meV; Lower panel: Calculated topological charge for opposite field-sweep directions (orange and black line). (e) Full up and down Hall-resistivity traces for device C ( $d = 2.4 \mu\text{m}$ ) recorded at 300 K. Inset: Reduced-area plot. Arrows indicate the field-sweep direction. Red dashed line is a linear fit. (f) Magnetization for a bulk sample and device C, recorded before it was structured into a Hall bar by FIB. Inset: Reduced-area plot. (g) Differences between up and down sweeps for the Hall and magnetization data shown in (e) and (f), respectively. Insets: Background-subtracted component related to the field region where ASKs are detectable.



**FIG. 3. Thickness and temperature dependence of the magnetic textures and Hall component associated with ASKs.** (a) MFM images (local magnetic  $z$  component represented by  $\Delta\phi$ ) showing chiral domains and an ASK lattice for two samples prepared by FIB patterning with thicknesses of 5 and  $1.5 \mu\text{m}$ . The data were recorded at room temperature in zero-field and at 550 mT applied parallel to the  $c$  axis, i.e., parallel to the line of sight. The lower panels show the respective FFTs (in arb. unit with logarithmic color scale). (b) ASK Hall component,  $\rho_{xy}^{\text{ASK}}$ , plotted against magnetic field for devices B, C, E, and G with thicknesses of 1, 2.4, 0.7, and  $0.8 \mu\text{m}$ , respectively. (c) Thickness dependence of  $\rho_{xy}^{\text{ASK}}$  compared to the domain periodicity,  $w$ , determined by recent MFM measurements [22, 27]. The error bars represent the standard deviation of the values for variations in the details of the background subtraction. (d)  $\rho_{xy}^{\text{ASK}}$  for temperatures between 10 and 300 K for device B with  $d = 1 \mu\text{m}$ . (e) Maximum amplitude of  $\rho_{xy}^{\text{ASK}}$  in device B ( $d = 1 \mu\text{m}$ ) plotted against temperature. Red dots are a guide to the eye. The error bars are defined as in (c). (f) Temperature dependence of the maximum difference in the Hall-resistivity loop,  $\Delta\rho_{xy}$  between up and down sweeps for devices A, B, and E.

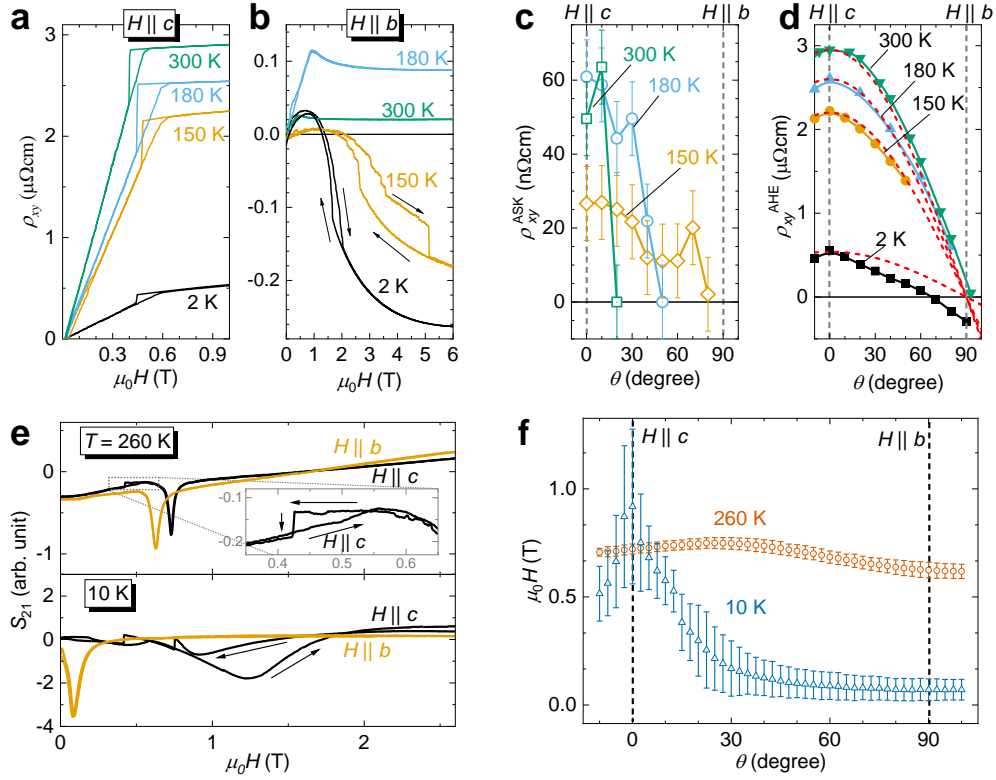


FIG. 4. **Angle-dependent Hall and FMR at various temperatures.** (a), (b)  $\rho_{xx}(H)$  of device B with  $1\,\mu\text{m}$  thickness recorded for  $H \parallel c$  and  $H \parallel a$ , respectively, at various temperatures. (c) Extracted ASK Hall signature at three fixed temperatures for various angles. The error bars are defined as in Fig. 3c. (d) Anomalous Hall coefficient extracted from linear fits to the high-field part above 5 T of  $\rho_{xy}(H)$  plotted against the tilt angle  $\theta$ . Red dashed lines are fits with  $\rho_{xy}(H) \propto \cos\theta$ . (e), (f) FMR forward-transmission parameter,  $S_{21}$ . (e) FMR spectra for  $H \parallel c$  and  $H \parallel b$  recorded for a  $0.8\,\mu\text{m}$  thick lamella at 10 and 260 K. (f) Angular dependence of the FMR field. Error bars represent the resonance linewidth values.

# Supplementary Materials for

## **Antiskyrmions and their electrical footprint in crystalline mesoscale structures of $\text{Mn}_{1.4}\text{PtSn}$**

Moritz Winter, Francisco J.T. Goncalves, Ivan Soldatov, Yangkun He, Belén E. Zúñiga Céspedes, Peter Milde, Kilian Lenz, Sandra Hamann, Marc Uhlarz, Praveen Vir, Markus König, Philip J. W. Moll, Richard Schlitz, Sebastian T. B. Gönnenwein, Lukas M. Eng, Rudolf Schäfer, Joachim Wosnitza, Claudia Felser, Jacob Gayles\*, and Toni Helm\*\*

\*Corresponding author. Email: [gayles@fsu.edu](mailto:gayles@fsu.edu)

\*\*Corresponding author. Email: [t.helm@hzdr.de](mailto:t.helm@hzdr.de)

### **This PDF file includes:**

Supplementary Notes 1 to 9  
Supplementary Figures 1 to 16

### **Other Supplementary Materials for this manuscript include the following:**

Supplementary Movie 1



## Supplementary Note 2. FIB-microstructure devices examined in this work

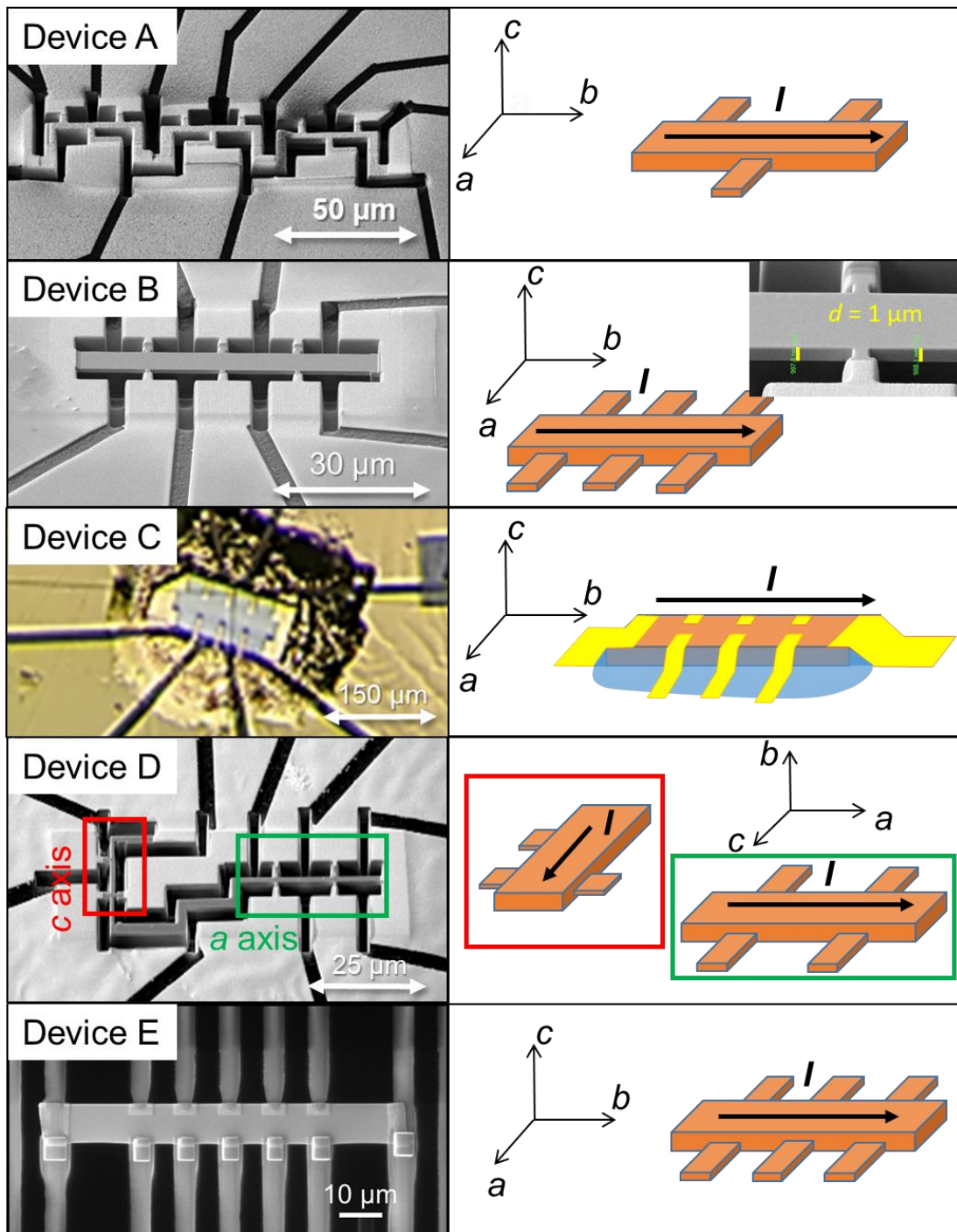


**Fig. S2. Different FIB-microstructure designs used in our study (see text below).**

In this study, we investigated the transport properties of more than 5 different devices, covering various thicknesses and designs. In Fig. S2, we show SEM images of **devices A to E** (left) and



sketches of the respective contact designs (right). Note: **Device F**, shown in Fig. 2d and in the Supplementary Movie sequence, is not shown here.

**Device A** (also shown in Fig. 1b in the main text) is a meander-shaped Hall-bar device, divided into steps with different thicknesses, namely  $d = 11.2, 8.4, \text{ and } 2.7 \mu\text{m}$ . We chose this design to allow for simultaneous measurements on different material thicknesses. The crystallographic  $c$  axis is oriented out of plane and the current is applied within the  $ab$  plane. Another characteristic of the structure is the particular arrangement of the electrical contacts. For each thickness, there are three contacts, two on one side and one centered on the opposite side. When measuring on opposite sides, the measured signal is a superposition of  $\rho_{xx}(H)$  and  $\rho_{xy}(H)$ . The latter is antisymmetric to magnetic field, and, hence, can be separated numerically after measuring both components simultaneously via one diagonal contact pair. We have fabricated various microstructures from  $\text{Mn}_{1.4}\text{PtSn}$ , individually tailored to serve specific tasks.

**Devices B, C, E, and F** were designed in a classic Hall-bar configuration, with opposing voltage contacts on each side. The  $c$  axis is oriented out of the plane.

**Device B** is a Hall-bar device with gold contacts (similar to **devices A, C, D, and F**), deposited on top of a  $1.0 \mu\text{m}$  thick lamella fixed by a droplet of epoxy. The approximately  $100 \text{ nm}$  thick gold film was etched locally into separate leads with the help of Ga ions.

**Device C** is a Hall-bar device with  $d = 2.4 \mu\text{m}$ . We did not cut into the lamella and only deposited gold contacts on top.

**Device D** is a series connected Hall-bar device with the  $b$  axis, i.e., the  $[010]$  direction, oriented perpendicular to the substrate surface. In the two series-connected sections with thickness  $d = 1.6 \mu\text{m}$ , the current is forced along the  $a$  axis and along the  $c$  axis, respectively. This enables a simultaneous Hall measurement of both current configurations.

**Device E** is a Hall-bar device with  $d = 0.7 \mu\text{m}$ . (A similar **device F** with  $d = 0.8 \mu\text{m}$  was produced in the same way for the results presented in Fig. 1e and d, and in the video). The lamella was transferred onto a glass substrate without additional glue or epoxy. Platinum contacts were deposited on the sides by the help of a FIB gas-injection system, providing connections to gold leads on the glass substrate that were fabricated by sputter deposition.

### Supplementary Note 3. Basic transport characterization

When examining structures produced by FIB milling, it is important to ensure that the physical properties of the material stay unaltered. Typically, the modification process with Ga ions leaves an amorphized, only few nanometer-thick layer on the surface of the specimen. The implantation of Ga ions depends on the acceleration voltage. The typical value of 30 eV gives rise to primary and secondary effects penetrating the surface with a maximum depth of 10-20 nm. For metallic materials used in devices with micron thicknesses, the electrical properties are preserved, since the major part of the current flows through the damage-free part of the sample. In addition, inhomogeneous mechanical stress may affect the devices, specific for each design. As we will exemplify in the following, the main transport characteristics, such as the temperature and field dependence of the resistivity and the Hall effect are not altered as compared to the results previously reported for bulk single crystals, see Vir et al. [29].

Fig. S3 shows  $R(T)$  for  $j \parallel a$  and  $j \parallel c$  measured simultaneously in device D. In comparison to a bulk sample the overall  $T$  dependence of  $R$  is preserved. Furthermore, the resistivity anisotropy remains very weak. Only slight variations between the two current directions are observed that may indicate weak differences in the experienced stress induced by the coupling to the substrate. Nevertheless, the striking feature, i.e., the kink in the slope at the spin-reorientation transition temperature,  $T_{\text{SR}} \approx 170$  K, is not altered (see also Fig. S4).

In Fig. S5, we exemplify the magnetoresistance (MR) in relative units and the Hall resistivity measured on device D for the two distinct transport directions,  $j \parallel a$  and  $j \parallel c$ . It matches previously reported bulk data [29, 33]. Both transport channels exhibit an overall negative MR of a few percent in magnitude for the full  $T$  range between 2 and 300 K. At low fields, below the saturation field  $\mu_0 H_s \approx 1$  T, variations of the slope are observable, likely related to the helical phase. Once we cool down to below  $T_{\text{SR}}$ , this anomaly grows significantly. In contrast, for  $H \parallel c$  (realized for device B) the MR changes to an almost linear field dependence once  $T < T_{\text{SR}}$ .

The low-temperature Hall resistivity (see 150 and 2 K in Fig. S5) exhibits a broad hump for fields below 3 T aligned within the  $ab$  plane, matching with previous reports for bulk single crystals [33]. This hump is associated with the topological Hall contribution due to the noncoplanar magnetic phase, established below  $T_{\text{SR}}$ . For field aligned along the  $c$  direction, the Hall resistivity acquires a nonsaturating positive slope at high fields, above the sharp shoulder at  $H_s$  accompanied with a small hysteresis as we describe in the main text (see Fig. 1c). This hysteretic behavior only emerges in thin devices and intensifies the lower the thickness, as we discuss in the main text.

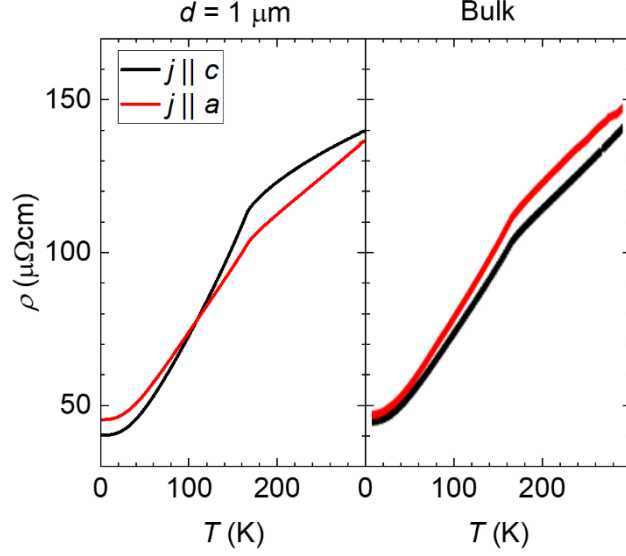


**Fig. S3. Zero-field resistivity anisotropy.** Comparison of Device B with bulk data from ref. [29].

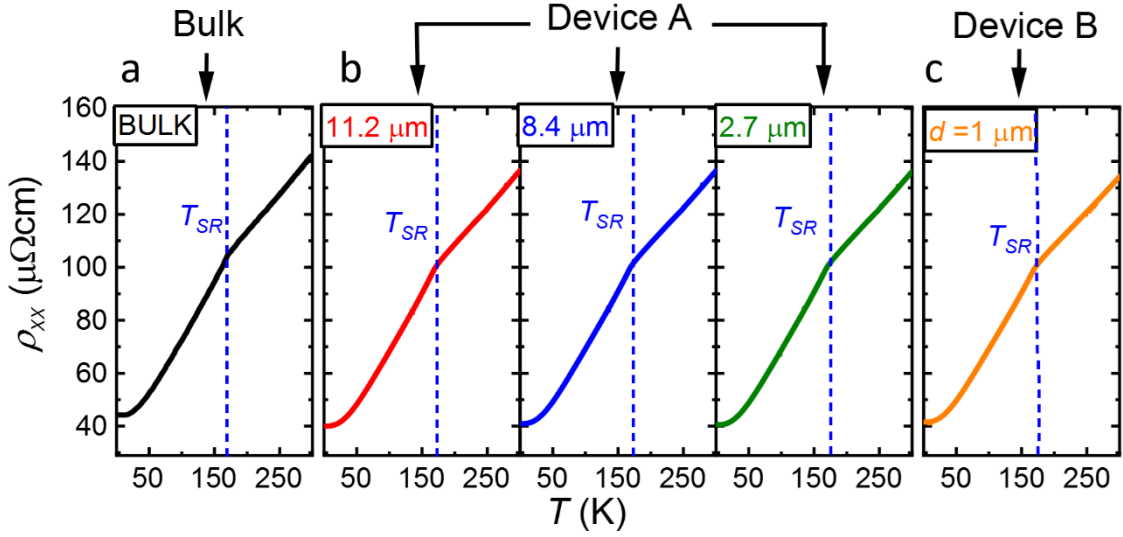


**Fig. S4. Temperature dependence of the zero-field resistivity.** (a) Bulk data from reference Vir et al. [29] (b), (c) Data recorded for devices A and B, respectively. The former has three series-connected Hall-bar devices with varying thickness.

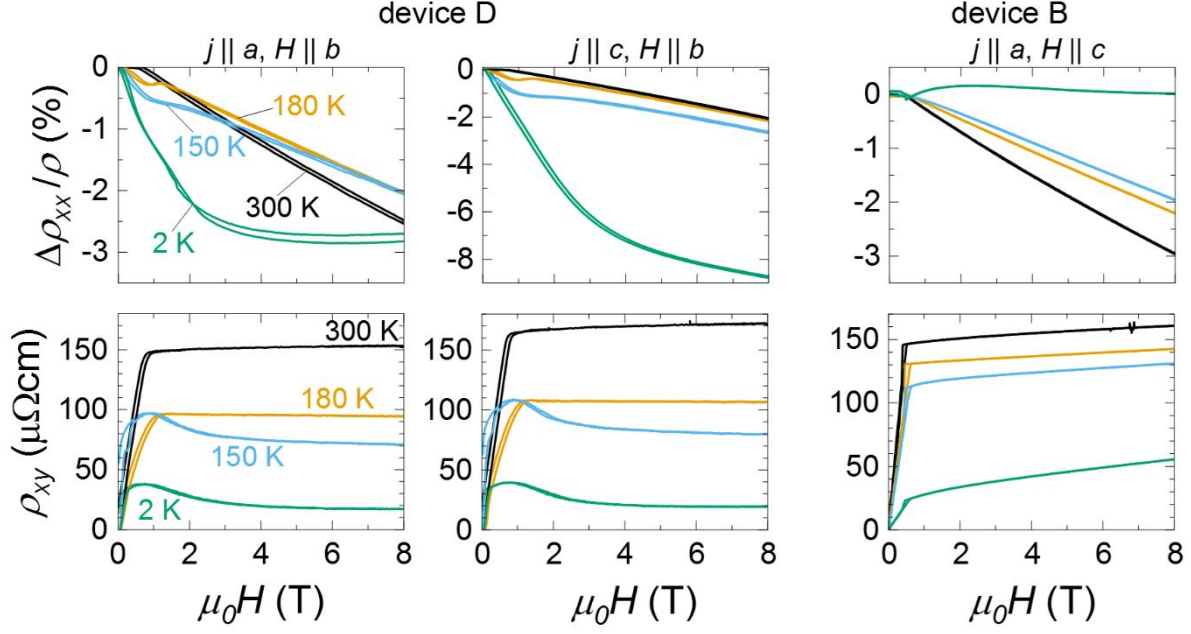


**Fig. S5. Magnetotransport anisotropy of devices D and B** recorded at four different temperatures with field aligned along the  $a$  and  $c$  direction, respectively. Upper and lower panels show respectively the magnetoresistivity and the Hall resistivity versus magnetic field.

#### Supplementary Note 4. Magnetization of a thin, lamella-shaped sample of $\text{Mn}_{1.4}\text{PtSn}$

A reliable measurement of the magnetization is not feasible for the microstructured devices due to their small volume. Nevertheless, the basic magnetic behavior of the material is important for understanding the magnetotransport experiments. In particular, the analysis of the anomalous Hall effect,  $\rho_{xy}^{\text{AHE}}$ , which is proportional to the magnetization, is needed for disentangling the various Hall effects. In Fig. S6, we present magnetization data recorded for a FIB-cut lamella with  $(a \times b \times c) = (60 \times 160 \times 2.4) \mu\text{m}^3$ , which was later used to fabricate device C. We performed the measurements in a Quantum Design 7 T SQUID magnetometer. For  $H \parallel c$ , we observe a hysteresis close to the saturation field (see Fig. S6a). This feature is similar to what we observed in the magnetotransport of the device shown in the main text in Fig. 1c and e. It, however, does not occur in bulk samples [29]. Below  $T_{\text{SR}}$ , we also observed a hysteresis for a high tilt angle of  $85^\circ$  off the  $c$  axis towards the  $a$  axis (see Fig. S6b). Note: The 310 K difference plot in Fig. S6c exhibits two maxima, which indicate a nonuniform thickness of the thin (but large in area) lamella sample. This may affect the nucleation process of the chiral domains in the magnetizing loop, on the way back to zero. Indeed, we were able to confirm this feature by Kerr-effect measurements on the same lamella (see Supplementary Note 5).

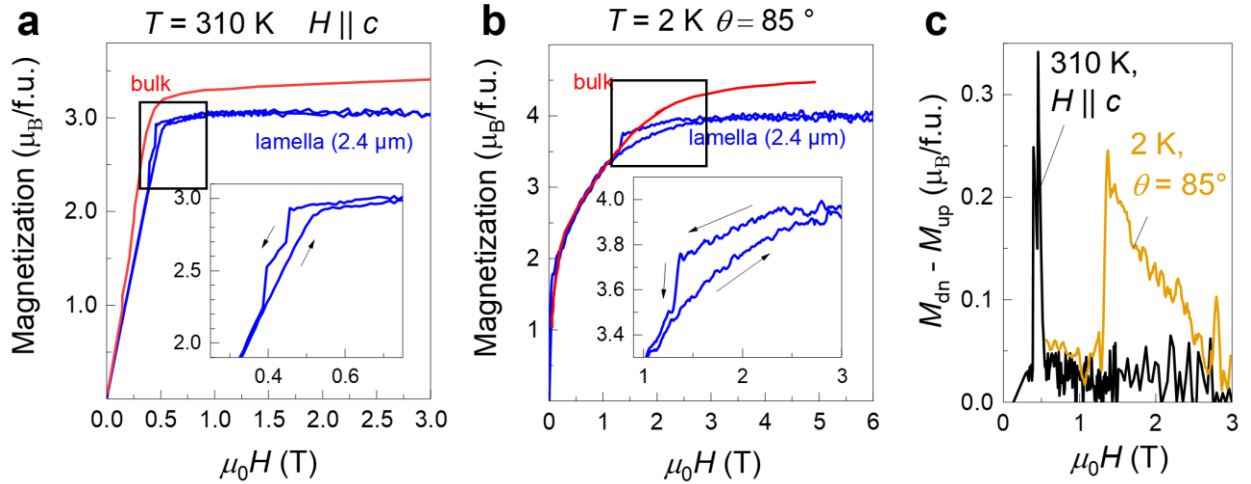


**Fig. S6. Magnetization for a  $2.4 \mu\text{m}$  thick lamella of  $\text{Mn}_{1.4}\text{PtSn}$ .** (a), (b) Magnetization data recorded at (a)  $T = 310 \text{ K}$ , with  $\theta = 0^\circ$  (i.e.,  $H \parallel c$ ), and (b)  $T = 2 \text{ K}$ , with  $\theta = 85^\circ$ . Device C was fabricated from this sample. Insets are zoomed into the hysteretic region. (c) Hysteresis in the magnetization. Difference between up and down field sweep for (a) and (b).

## Supplementary Note 5. Polar magneto-optical Kerr effect (MOKE) details

For our MOKE experiments, we transferred thin platelets prepared by FIB into a glue droplet on a glass substrate. We reduced the amorphized surface-layer thickness by an additional Ar-ion etching step afterwards. Low Ar-plasma voltages of the order of 1 kV keep the impact-layer thickness to a few nanometers. We exemplify the MOKE imaging process recorded for the 2.4  $\mu\text{m}$  thick sample that was used later on for device C. First, we recorded a background image in the field-polarized state, where no magnetic textures are visible any more. The background is then subtracted from each image taken at lower fields in order to better visualize the field-induced contrast changes.

In Fig. S7, we present a series of MOKE images collected for device C. A water-cooled electromagnet was used. The sample was sitting at a distance of approximately 5 mm above the pole of the magnet. Therefore, the absolute field at the sample level should be scaled by a factor 0.8. Starting from zero, the field was increased to +700 mT, in steps of 10 mT, where we took an image that was used as reference background. Next, we went back to zero, further to -700 mT, and back to +500 mT keeping the same step size. At 500 mT, we continued at a slower pace with 1 mT steps until +700 mT and returned to zero. During this slow field-stepping process the focus and contrast was manually adjusted to compensate for slight drifts. Figure S7a shows how the band domains slowly disintegrate into dot-like objects that assemble in a hexagonal structure at around 571 mT. This is exactly the point when the shoulder feature in the Hall effect emerges. As we further increase the field, these points remain fixed and gradually reduce in size until they vanish within the background noise. This suggests that these objects are no simple bubbles. The clear negative sign of the AHE provides strong evidence for ASKs as the local magnetization of these objects should decrease due to the zero net magnetization of ASKs. Once we turn back to lower fields, the sample remains in the field-polarized state until suddenly (within less than a millitesla) band domains and only few dots reestablish. As the field approaches zero, these patterns turn into longer continuous bands and the distance/width is shrinking with increasing field.

Figure S8a-e shows Kerr-effect images of the whole lamella during the demagnetization, coming from the field-polarized regime. It can be clearly seen that the lamella is divided into two regions. While at 410 mT one region already shows the helical phase with domain bands along the *ab* direction, typical for  $\text{Mn}_{1.4}\text{PtSn}$ , the other half is still in the field-polarized state. At 390 mT, the hysteresis loop is complete and magnetic spirals have formed throughout the sample. This proves that the origin of the major hysteresis is related to the establishment of the helical spin-spiral phase. It also explains the double-step of the magnetization hysteresis for this particular sample, shown already above in Fig. S6c. In Fig. S8f, we show a zoomed-in version of the room temperature magnetization difference from Fig. S6c.

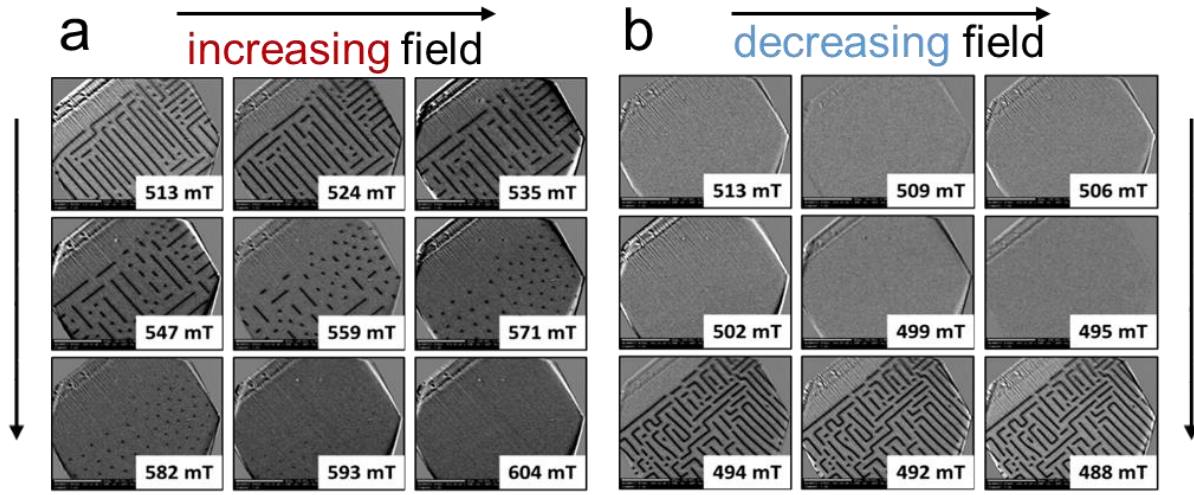


**Fig. S7.** MOKE image series recorded on device C with  $d = 2.4 \mu\text{m}$  at room temperature for selected field values in the vicinity of the hysteretic region. The given external magnetic field is the set field of the electromagnet (values need to be scaled by a factor 0.8 in order to take into account the distance between sample and magnet pole)

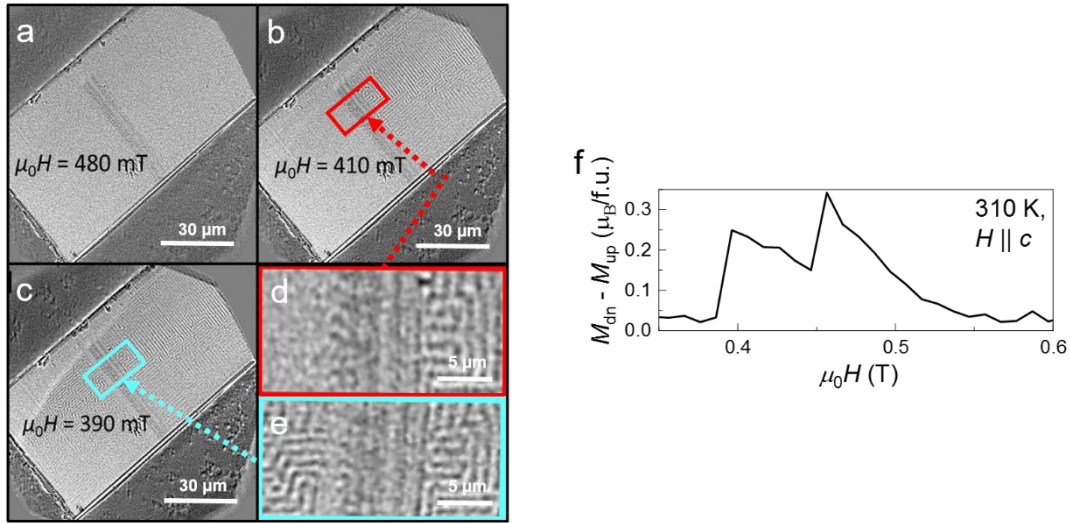


**Fig S8.** MOKE images recorded on device C in the hysteretic field range. Starting from zero the field was ramped to negative 600 mT, back to zero, to positive 600 mT and to (a) 480 mT, still in the field-polarized state; next to (b) 410 mT, where the helical band domain patterns are already observable in one half of the sample; and finally to (c) 390 mT, where the helical phase is observable in both parts. (d), (e) Zoomed-in images of the marked regions in (b) and (c), respectively. (f) Zoomed-in magnetization difference between up and down field-sweep at room temperature (with  $H \parallel c$ ) shown already above in Fig. S6(c).

## Supplementary Note 6. Atomistic spin-dynamic simulations

The origin of the noncollinear magnetic textures is due to a competition of classical exchange interactions between the inter-site interactions of the magnetic atoms Mn1 and Mn2 (with Wyckoff positions  $4a$  and  $8d$ , respectively) and the intra-site interactions. This can be modeled by a classical exchange Hamiltonian

$$H_{\text{exch}} = -J_1 \sum_{\langle ij \rangle, l, l'} (\mathbf{s}_i^l \cdot \mathbf{s}_j^{l'}) (1 - \delta_{l, l'}) - J_2 \sum_{\langle ij \rangle, l, l'} (\mathbf{s}_i^l \cdot \mathbf{s}_j^{l'}) (\delta_{l, I} \delta_{l, l'}) \\ - J_3 \sum_{\langle ij \rangle, l, l'} (\mathbf{s}_i^l \cdot \mathbf{s}_j^{l'}) (\delta_{l, II} \delta_{l, l'}).$$

Here,  $\mathbf{S}_i$  is the unit vector of spin for each sublattice ( $I$ ),  $J_1$  is the inter-sublattice interaction, and  $J_2$  and  $J_3$  are the  $8d$  Mn2 and  $4a$  Mn1 intra-site interactions for each sublattice, respectively. All interactions together are necessary for a noncollinear spin texture. The positive  $8d$  Mn2 interactions,  $J_2$ , align the spins parallel and are the largest contribution to the ordering temperature. The  $4a$  Mn1 interactions,  $J_3$ , are negative, which favors an antiparallel alignment. Lastly, the inter-site interaction,  $J_1$ , is positive and causes a noncoplanar magnetic structure depending on the relation with the other interactions. When  $J_1$  is weak ( $J_1 < \frac{1}{4} J_2$ ), the coupling between the  $8d$  Mn2 and  $4a$  Mn1 sublattice is weak, and the noncoplanar structure stabilizes as the ground state. When  $J_1$  is strengthened, the  $4a$  Mn1 sublattice follows that of the  $8d$  Mn2 sublattice for a collinear alignment and is, therefore, the origin of the spin reorientation. The DMI Hamiltonian is

$$H_{\text{DMI}} = \mathbf{D}_1 \cdot \sum_{\langle ij \rangle, l, l'} (\mathbf{s}_i^l \times \mathbf{s}_j^{l'}) (1 - \delta_{l, l'}) + \mathbf{D}_2 \cdot \sum_{\langle ij \rangle, l, l'} (\mathbf{s}_i^l \times \mathbf{s}_j^{l'}) (\delta_{l, I} \delta_{l, l'}) \\ + \mathbf{D}_3 \cdot \sum_{\langle ij \rangle, l, l'} (\mathbf{s}_i^l \times \mathbf{s}_j^{l'}) (\delta_{l, II} \delta_{l, l'}),$$

where  $\mathbf{D}_2$  and  $\mathbf{D}_3$  are nominally equal and opposite. Lastly, the effective uniaxial-anisotropy field and the external magnetic field are modeled by

$$H_{\text{field}} = -k_u \sum_{i, l} (\mathbf{s}_i^l \cdot \mathbf{e})^2 - \sum_i \mu_s \mathbf{S}_i \cdot \mathbf{H}_{\text{ext}}.$$

$k_u$  is the uniaxial anisotropy constant and  $\mathbf{H}_{\text{ext}}$  is the external field. The total Hamiltonian is the sum of the previously mentioned contributions  $H_{\text{tot}} = H_{\text{exch}} + H_{\text{DMI}} + H_{\text{field}}$ . We map these interactions onto the atomistic Landau-Lifshitz-Gilbert equation

$$\frac{\partial \mathbf{S}_i}{\partial t} = -\frac{\gamma}{1 + \lambda^2} [\mathbf{S}_i \times \mathbf{H}_{\text{eff}}^i + \lambda \mathbf{S}_i \times (\mathbf{S}_i \times \mathbf{H}_{\text{eff}}^i)].$$

The gyromagnetic ratio is  $\gamma$  and  $\lambda$  is the microscopic damping.  $\mathbf{H}_{\text{eff}}^i = -\frac{1}{\mu_s} \frac{\partial H_{\text{tot}}}{\partial \mathbf{S}_i} + \mathbf{H}_{\text{th}}^i$  is the effective field with thermodynamic fluctuations ( $\mathbf{H}_{\text{th}}^i$ ) modeled by Langevin dynamics and  $H_{\text{tot}}$ , which includes the exchange interactions, a uniaxial anisotropy and the external magnetic field. Within the vampire code [33, 53], we simulate a  $50 \times 50$  nm trilayer of  $\text{Mn}_{1.4}\text{PtSn}$  for periodic boundary conditions in the  $a$  direction and an open boundary in the  $b$  and  $c$  crystal axis. The lattice constant is chosen to be 0.2715 nm. In Fig. S9, we plot the  $M(H)$  loops of the spin texture as a function of the field along the  $c$  direction for both polar angles (top) and azimuthal angles (bottom). In high field, the ASK state begins to form. In Fig. S10, we show similar plots of the skyrmion state as a function of temperature and field.



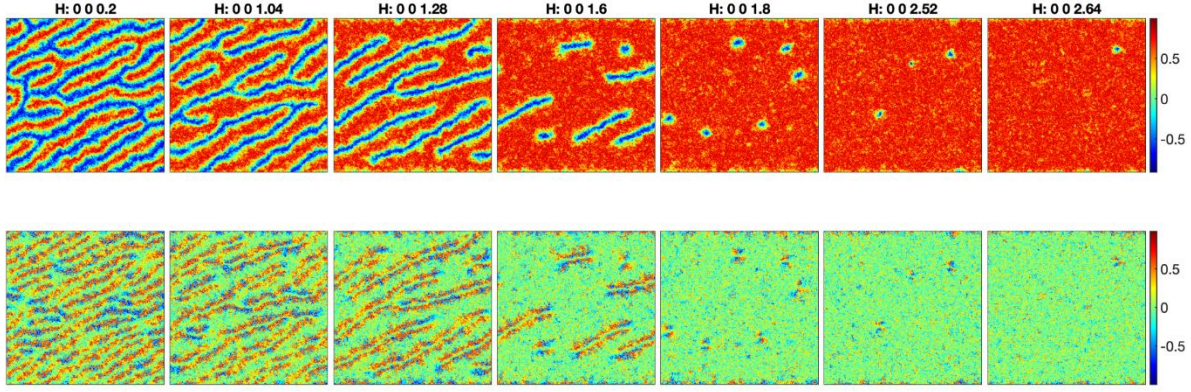


**Fig. S9. Spin configurations for an increasing-field sweep of  $\text{Mn}_{1.4}\text{PtSn}$  model.** For the polar angle,  $\theta$  we plot the contour density of each spin (top row) as  $\cos(\theta)$ , correspondingly for the azimuthal angle,  $\varphi$  we plot it (bottom row) as  $\sin(\varphi)$ . The color red marks spins that align with the magnetic field, whose direction points out of the plane and blue marks spins pointing into the plane. In a field range between 1.6 and 2.6 T the ASK state forms from the low-field helical phase and is destroyed at higher field. The ASK state is confirmed by the pin-wheeled shape of the azimuthal plots, where red and blue mark positive and negative in-plane components.

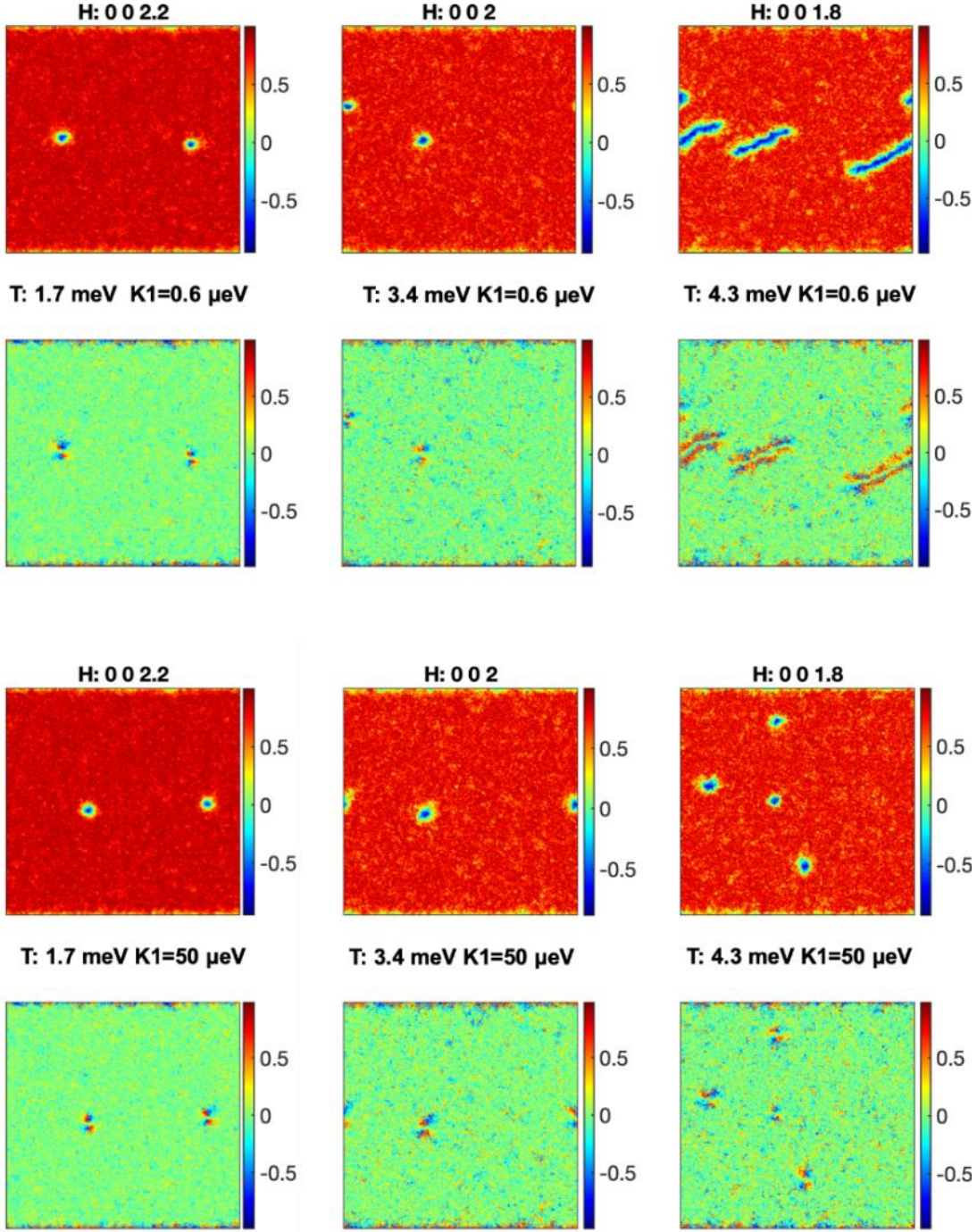


**Fig. S10.** Calculated ASK states as a function of two uniaxial anisotropy constants ( $K_1 = 0.6$  and  $50 \mu\text{eV}$ ) and three temperatures ( $T = 1.7, 3.4, 4.3 \text{ meV}$ ). For the polar angle,  $\theta$  we plot the contour density of each spin as  $\cos(\theta)$ , correspondingly for the azimuthal angle,  $\varphi$ , we plot  $\sin(\varphi)$ . For larger anisotropy the ASK state becomes more stable.

## Supplementary Note 7. Extraction of the ASK Hall-resistivity component

In order to extract the antiskyrmionic contribution to the Hall effect,  $\rho_{xy}^{\text{ASK}}$ , we need to determine the ordinary (orbital) and anomalous (magnetic) components,  $\rho_{xy}^{\text{OHE}}(M)$  and  $\rho_{xy}^{\text{AHE}}$ , respectively (see Eq. 1 in the main text). The first can be obtained from the high-field slope in the saturated (polarized) state.  $\rho_{xy}^{\text{AHE}}(M)$  is proportional to the magnetization,  $M(H)$ . However, due to the tiny volume of the microstructured devices, and thus the hardly resolvable magnetic moment, we had to choose another approach. As we have shown in Supplementary Note S4, we observe a hysteresis in the magnetization in a thin platelet of  $\text{Mn}_{1.4}\text{PtSn}$ . Apparently, there is a direct relation to the Hall response. In Fig. S11, we show four Hall-response examples recorded at 300, 180, 150, and 2 K. Interestingly, there is a shoulder-like feature in the up sweeps right before saturation is reached. Supported by polar MOKE microscopy and MFM measurements we attribute this to the formation of the ASK lattice and the associated  $\rho_{xy}^{\text{ASK}}$ .

With increasing field, the ASK lattice establishes from the helical phase at field  $H_{c1}$ . It is stable up to the transition to the field-polarized state at  $H_{c2}$ . As we decrease the field, no spin textures are observed in the MOKE measurements until the hysteresis closes. Thus, the difference  $\Delta\rho_{xy}$  directly reflects the influence of the spin textures compared to the field-polarized state (see Fig. S11c, d). Our in-situ measurements in combination with MOKE on devices C and E provide unambiguous evidence for the ASK lattice as the origin of this sudden change in the Hall signal. We associate this feature with the ASK Hall-resistivity component. As the topological charge for these magnetic excitations is opposite to that of Bloch- and Néel-type skyrmions a negative THE is expected. However, its magnitude is expected to be very small because of the huge dimensions of the ASKs for micron-thick devices. We also show in the main text for the example of a  $2.4\ \mu\text{m}$  thin sample that there also seems to be a signature in the magnetization (Fig. 2g). Unfortunately, it is already within the noise for this unstructured relatively large lamella-shaped sample, and, hence, was not resolvable for thinner structured devices. We extract  $\rho_{xy}^{\text{ASK}}$  from  $\Delta\rho_{xy}$  by subtracting off a linear fit as demonstrated in Figs. S11c, d, e, and f. Here, we also present the magnetoresistivity data. Although the overall magnitude with  $10^{-3}\%$  is rather small, we observe a hysteretic feature as well. Similar to the magnetization, no separate feature is discernible in the respective field range where ASKs are detected, marked by the yellow regions in Fig. S12. For temperatures below  $T_{\text{SR}}$ , where the noncoplanar phase is completely dominant, the overall hysteretic behavior reduces and additional step-like changes occur.

Figure S12 shows the extracted  $\rho_{xy}^{\text{ASK}}$  over the entire temperature range studied. Above 170 K, the picture is consistent and the shoulder-like feature can be distinctively traced. However, below and down to base temperature we cannot directly link our data to ASKs. It becomes clear that  $T_{\text{SR}}$  has a significant effect on the ASK signature. It recently has been demonstrated for electron-transparent lamellas that at low temperature Bloch-type skyrmions emerge [18]. The presence of skyrmionic textures with varying net magnetizations or topological winding would result in compensating/varying AHE and THE components. The schematic temperature dependence of the ASK region is highlighted in Fig. S13a. MFM confirmed ASKs for temperatures as indicated (blue diamonds) above  $T_{\text{SR}}$ . Further detailed magneto-optical measurements are necessary to reveal the origin of the observed low-temperature behavior.

In Fig. S13b, we show  $\rho_{xy}^{\text{ASK}}$  extracted for device B with  $1\ \mu\text{m}$  thickness at various angles and at  $T = 180$  and  $150\ \text{K}$ . Apparently, the ASK Hall-resistivity contribution is maintained also for tilts away from  $H \parallel c$ . Even at  $150\ \text{K}$ , we were able to trace it until  $70^\circ$  tilted off the  $c$  direction.

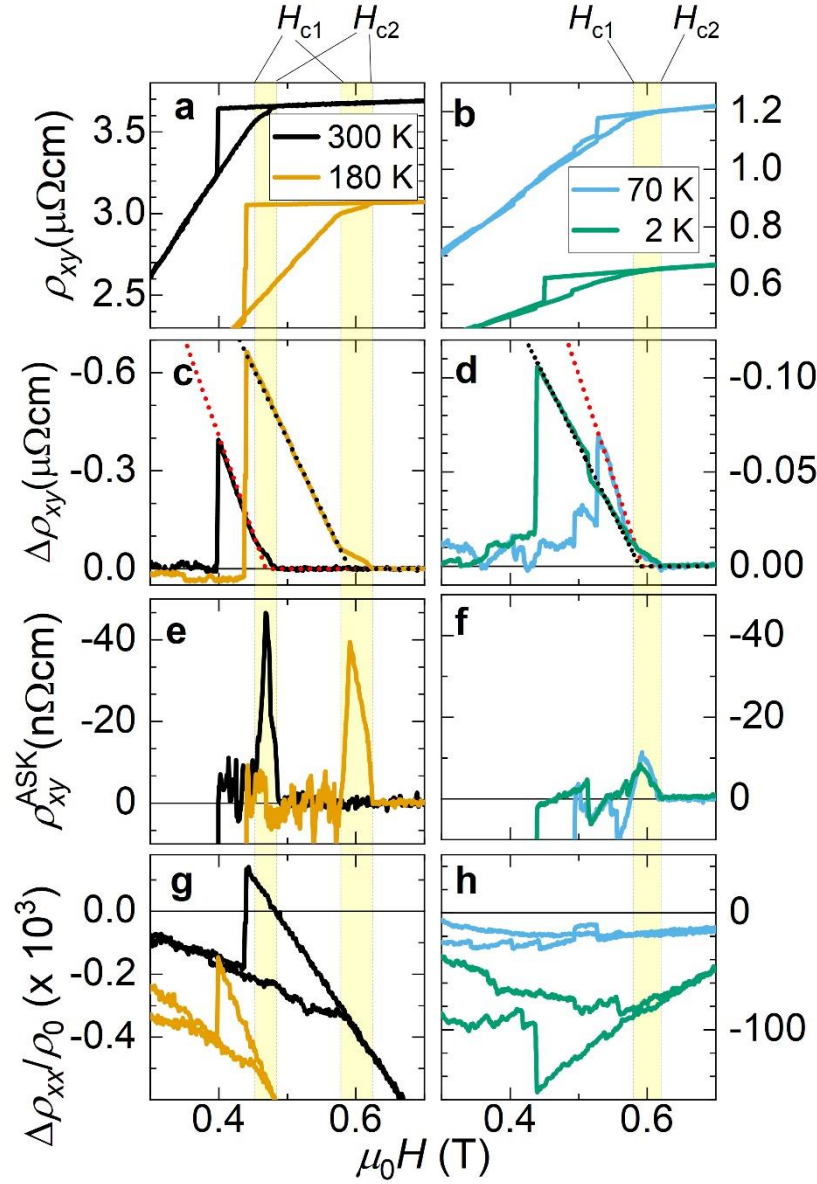


**Fig. S11. Hall-component extraction for the 1  $\mu\text{m}$  device B.** (a), (b) Hall resistivity at  $T = 300$ , 180, 70, and 2 K. (c), (d) Difference between up and down sweep of the data shown in (a), (b). (e), (f) difference between linear fits shown as dotted lines in (c), (d) and  $\Delta\rho_{xy}$ . (g), (h) Magnetoresistance scaled by a factor of 1000.



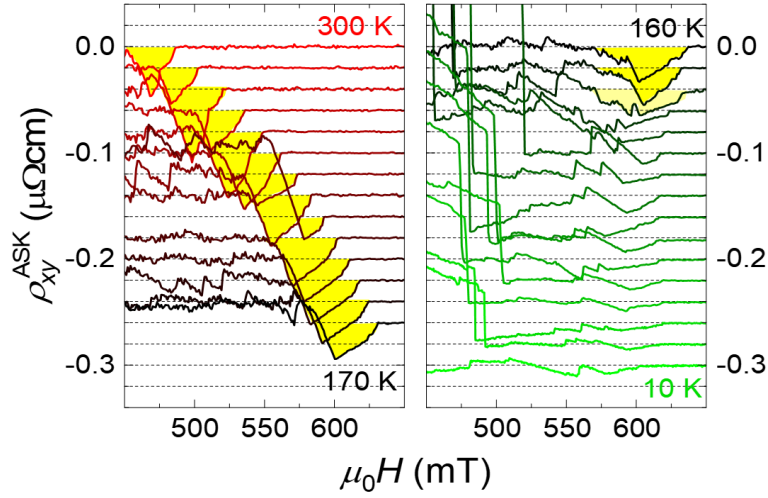


**Fig. S12 Temperature dependence of the ASK Hall-resistivity component for device B.** ASK Hall-resistivity component,  $\rho_{xy}^{\text{ASK}}$ , extracted for device B at various temperatures.

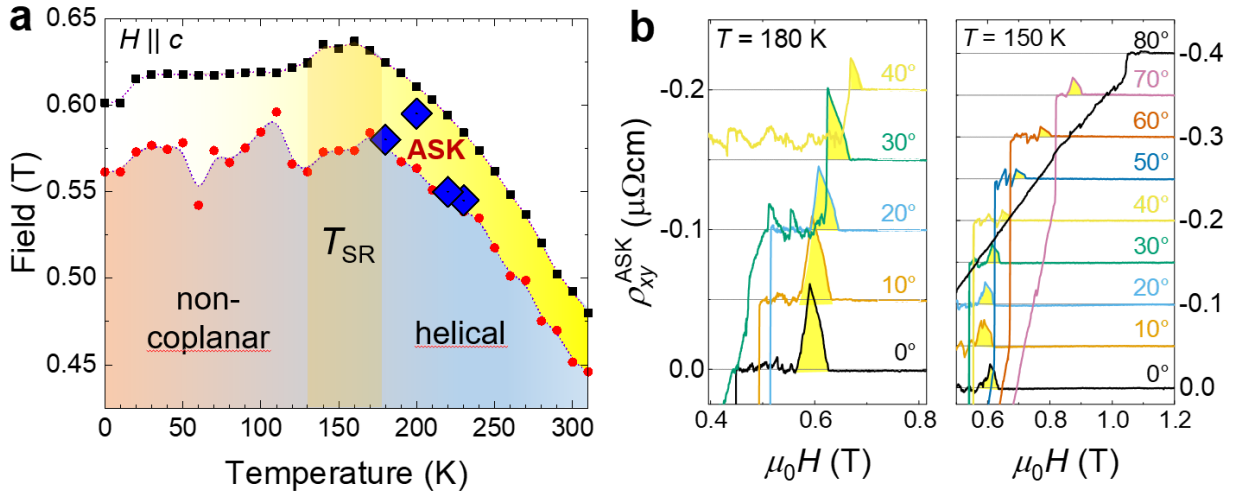


**Fig. S13. Schematic phase diagram and angle dependence of the ASK Hall component for device B.** (a) Black and red dots mark the field value at which  $\rho_{xy}^{\text{ASK}}$ , presented in Fig. S12, starts deviating from zero. The blue diamonds mark temperature and field values at where we confirmed the presence of an ASK lattice by MFM in a 1  $\mu\text{m}$  thick sample. (b)  $\rho_{xy}^{\text{ASK}}$  extracted at 180 and 150 K for various angles.

**Estimate of the THE component:**

The Hall resistivity linked to the emergent field  $H^e$  induced by the ASK phase may be estimated by [13]:

$$\rho^{THE} = -P \cdot R_0' \cdot (n^{ASK} \cdot \Phi_0),$$

where  $P$  is the spin polarization of the charge carriers,  $R_0'$  is the Hall coefficient representing the effective charge density contributing to the THE of spin-up and spin-down carriers, and  $n^{ASK}$  is the antiskyrmion density and  $\Phi_0 = h/e$  is the magnetic flux quantum.  $R_0$  is derived from the difference of spin-up and spin-down contributions. A rough estimate was already provided by calculations [33].  $R_0$  for  $\text{Mn}_{1.4}\text{PtSn}$  was calculated to  $0.5 \cdot 10^{-8} \Omega\text{cm/T}$ . The experimental value, determined from the slope of the Hall resistivity in fields above 2 T at room temperature, is an order of magnitude larger with  $4 \cdot 10^{-8} \Omega\text{cm/T}$ . The ASK density for a 1  $\mu\text{m}$  thick device can be approximated to  $1/(100 \text{ nm})^2$ . Assuming a low spin-polarization value of  $\sim 0.1$  we would be able to attempt a rough estimate using the equation above. Hence, the expected THE component may be of the order of 1 n $\Omega\text{cm}$ , which is similar to what was observed for MnSi [13].

## Supplementary Note 8. Angle-resolved transport measurement

We investigated the Hall resistivity for various devices. In Fig. S14a, we show a detailed study of the angle- and field-dependent Hall resistivity conducted on device B with 1  $\mu\text{m}$  thickness. The measurements were realized as illustrated in Fig. S14b by performing a field sweep at an angular configuration and then increasing the tilt angle. As expected, the general intensity of the Hall signal decreases with higher tilt angles. However, the characteristic transport properties of the material are clearly visible. Particularly striking is the THE of the noncoplanar spin structure, which starts to develop at 180 K and becomes even stronger at lower temperatures. This manifests itself in an increasingly pronounced maximum at higher tilt angles. The overall Hall signal exhibits a peculiar temperature dependence: Its high-field slope changes sign for  $T < T_{\text{SR}}$  as the field orientation is approaching the in-plane direction. In Fig. 4d of the main text, we show the AHE component plotted against  $\theta$ . The deviation from the conventional  $\cos\theta$  dependence is a consequence of the slope change at low temperature.

For  $T < T_{\text{SR}}$ , a hysteresis in the Hall effect is observable at almost any field orientation, even close to  $H \parallel b$  ( $\theta = 90^\circ$ ). The hysteretic field range shifts to higher field values with increasing tilt angle away from the  $c$  direction. Figure S14c shows field sweeps with  $H$  close to the  $b$  direction. At 2 K, the hysteresis is particularly pronounced and small steps can be resolved in both up and down sweeps.

To highlight the distinct behavior of the hysteresis above and below  $T_{\text{SR}}$ , Fig. S15 shows plots of  $\Delta\rho_{xy}$  for 180 and 2 K. At 180 K, the peak due to the hysteresis is clearly visible (see Fig. S15a). To higher angles, there is a drastic reduction in the intensity of this peak until it disappears completely near  $80^\circ$ . To illustrate the disappearance of the peak and, hence, of the hysteresis at high tilt angle, Fig. S15b shows  $\Delta\rho_{xy}$  for field orientations close to  $H \parallel b$ . The behavior at 2 K shows distinct differences (see Fig. S15c). First, the magnitude of the peak in  $\Delta\rho_{xy}$  reduced. Second, a sign change of the peak occurs above  $80^\circ$  (see Fig. 15d). As the angle approaches the  $b$  axis, the intensity of the negative peak and the step field increase drastically. Once  $\theta$  passes  $90^\circ$ , the sign is reversed, which is expected from the sign change in the out-of-plane component of the field with respect to the current.

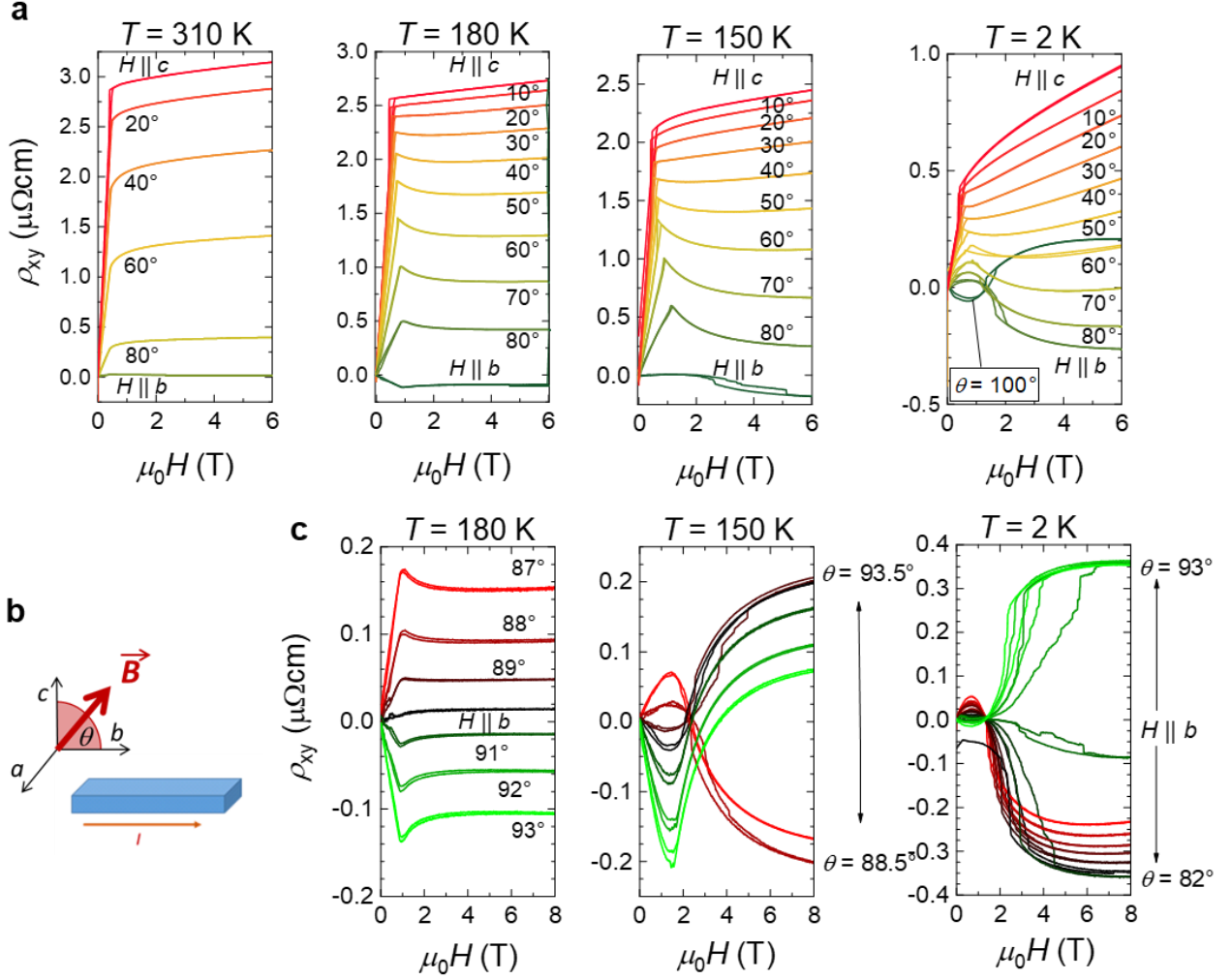


**Fig. S14. Angle- and temperature-dependent Hall resistivity of device B.** (a) Hall resistivity recorded for  $T = 310, 180, 150$ , and  $2 \text{ K}$  at various tilt angles. (b) Sketch of the sample configuration with respect to the current and field orientation. (c) Detailed Hall resistivity close to the in-plane orientation, i.e.,  $H \parallel b$ , recorded at  $180, 150$ , and  $2 \text{ K}$ .



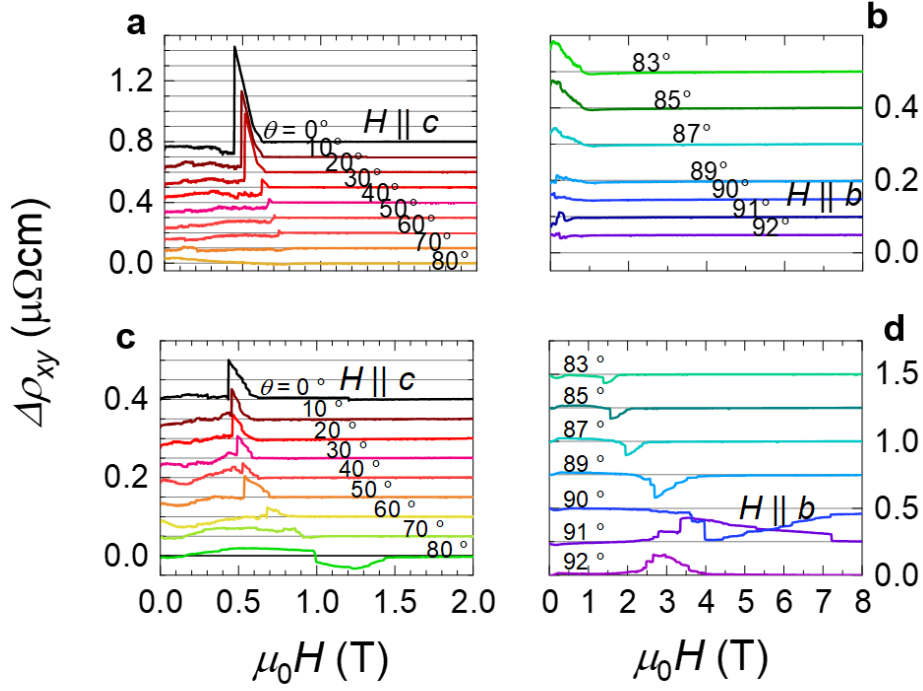


**Fig. S15. Angle dependence of the hysteretic part in the Hall effect.** Difference  $\Delta\rho_{xy}$  between the Hall resistivity for increasing fields  $\rho_{xy}^{up}$  and decreasing fields  $\rho_{xy}^{down}$  for measurements at different angles and the selected temperatures (a), (b) 180 K and (c), (d) 2 K.

## Supplementary Note 9. Ferromagnetic-resonance results

In order to learn more about the magnetic properties of the micron-sized samples, we looked for ferromagnetic resonances depending on temperature and angle. A thin FIB-cut and FIB-polished lamella was transferred ex situ onto the central lead of a coplanar waveguide on a silicon chip. The standard signature of a FMR absorption peak consists of a dip in the magnitude of the FMR forward-transmission parameter  $S_{21}$  that exhibits a Lorentzian-like shape when measured as a function of magnetic field. The center of the Lorentzian curve indicates the resonance field and the half width at half maximum linewidth. In other words, it represents the magnetic field that satisfies the resonance condition at the applied RF frequency (20 GHz). In Fig. S16, we exemplify FMR results for a thin  $\sim 800$  nm thick lamella of  $\text{Mn}_{1.4}\text{PtSn}$  for two temperatures,  $T = 260$  and 10 K, recorded for various field orientations between the  $c$  and  $b$  direction ( $\theta = 0^\circ$  and  $90^\circ$ ). Clearly, the main resonance exhibits a shift depending on the field orientation. At 260 K, we observe a sharp peak shifting slightly as we increase  $\theta$ , with a maximum at around  $25^\circ$  (black arrow in Fig. S16b). In contrast, at low temperature the main resonance is very broad for  $H \parallel c$  and exhibits a much stronger shift from approximately 1 T to 0.1 T as we rotate towards  $H \parallel a$ . This indicates strong changes of the magnetic anisotropy depending on temperature. The field asymmetry of the FMR spectra is consistent with the hysteretic behavior caused by the field-driven dynamics of the non-collinear magnetic textures (regardless of the nature of the textures), which is known to be asymmetric with regards to zero magnetic field. In order to extract the magnetic anisotropy constant,  $K$ , we used the FMR fields as indicated by the white circles in Fig. S16a. Lorentzian fits were performed for both  $+H$  and  $-H$  data, but only  $+H$  is plotted in Fig. S16b. For the fits to the 260 K data, we used a weak uniaxial anisotropy term and an in-plane cubic anisotropy term. Note that the cubic anisotropy is shifted by  $24^\circ$  with respect to the symmetry of the measurements. From these fits, we obtained  $K_{\text{uni}} = -7 \text{ kJ/m}^3$  and  $K_{\text{cubic}} = 110 \text{ kJ/m}^3$  (in-plane component). For the 10 K data, we approximated the divergence of the resonance at  $0^\circ$  by an out-of-plane uniaxial anisotropy term yielding an estimated anisotropy value  $K_{\text{uni}} = -630 \text{ kJ/m}^3$ . The interpretation of the FMR values is only sensitive to a net ferromagnetic magnetization of the frustrated magnetism in  $\text{Mn}_{1.4}\text{PtSn}$ . Nevertheless, we see a preferred in-plane orientation that can be affected by rather small changes of an external field, necessary for the formation of ASKs. Furthermore, the low-temperature results with higher effective anisotropy are in favor of the observed vanishing signatures of ASKs.

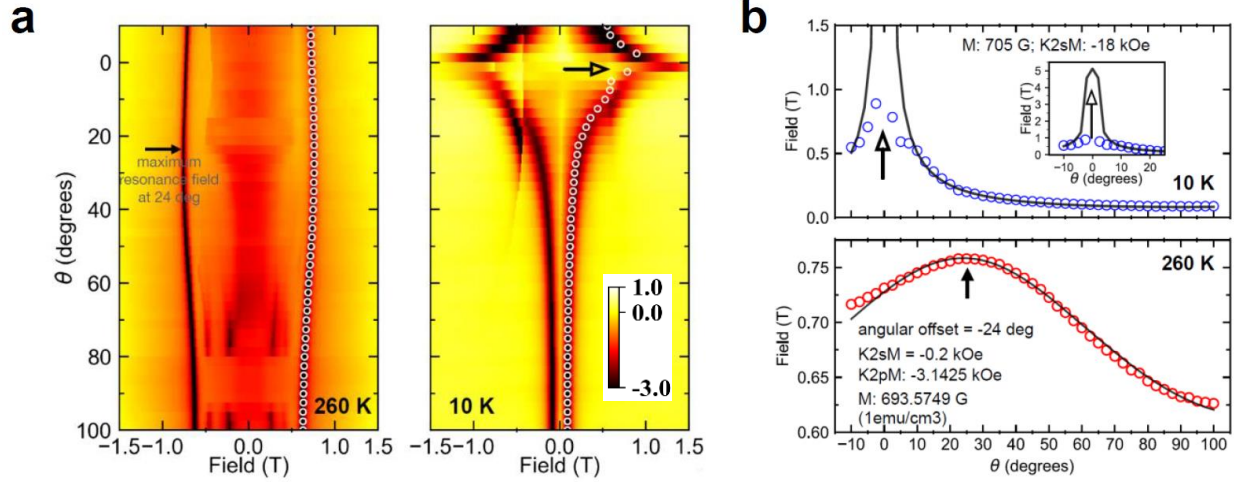


**Fig. S16. FMR above and below  $T_{SR}$ , at 260 and 10 K, respectively.** (a) Color maps of the FMR forward-transmission parameter,  $S_{21}$ , recorded for fixed frequency (20 GHz) and field ramps from negative to positive at various tilt angles  $\theta$ . White circles mark the resonance peak values used for our fits. (b) Resonance field plotted against the angle for 10 (blue) and 260 K (red). Black solid lines are fits. The inset shows the full fit for 10 K close to  $H \parallel c$ .